Hot subdwarfs stars in the Gaia era: A kinematic analysis

Masterarbeit aus der Physik

vorgelegt von Jasmina Henderson am 2. November 2018

Dr. Karl Remeis-Sternwarte Bamberg
Friedrich-Alexander-Universität Erlangen-Nürnberg

Betreuer: Prof. Dr. Ulrich Heber

Abstract

The recent Data Release of the Gaia mission provided new stellar data for billions of stars. The direct measurements of parallaxes from space based instruments have high precision which allow to minimize systematical errors even further. Hot subdwarfs of type O and B have been in focus for this research, especially the SPY sdO and sdB sample and the close binary sample taken from (Kupfer et al., 2015) which is a collection of binary systems with solved orbits.

Radial velocities of both SPY samples have been measured and four new RV variable stars have been detected. In a large scale kinematic analysis the impact of the chosen mass model of our Galaxy has been investigated. Therefore, three common models for the gravitational potential of our Galaxy have been analyzed while determining the stellar population distribution of the mentioned samples. Overall, only 2.1 % of the stars have been identified of a different stellar population depending on the chosen mass model. The stars of the SPY samples and the close binary sample have been categorized in different stellar populations with respect to their binarity. The overall distribution is the same for all samples. However, the SPY sdO samples has a higher percentage for halo candidates than the other samples.

Contents

1 Introduction

Observing and understanding the mechanics of the night sky has always been an intriguing task for mankind. Over thousands of years observational techniques improved and with every new kind of technology new theories have been proven and misconcepts have been clarified.

The Gaia mission started in 2013 with the goal to complete a thoroughly survey of the night sky and hereby circumventing the disadvantages of ground based observations such as light pollution, turbulences in the atmosphere and bad weather conditions. This mission is designed to measure parallaxes directly via trigonometry. Further stellar data such as position, proper motion and brightness have been measured as well with space based instruments. Already in the second data release Gaia provided trigonometric parallaxes for a huge number of stars with a precision better than 0.1 mas, which is better than previous mission by a factor of ten and more. The Gaia mission is designed to increase in precision over the years due to longterm observations which improves stellar data for the next data releases even further.

In our Galaxy are billions of stars with different characteristics. We categorize and generalize stars with common properties to understand their evolutionary stages. Some are more frequent than others and therefore more easily to research. Stars that belong to the group of hot subdwarfs are a minority, especially type O and B subdwarfs. Through measurements we gain stellar data about their surface temperature or their brightness, but they still need investigation. A kinematic analysis of hot subdwarfs gives insight about their distribution in our Galaxy and their rate of binaries, which helps to understand the evolutionary process of hot subdwarfs better.

In a large scale analysis three samples are kinematically investigated which are the SPY sdB and sdO sample and the close binary sample from Kupfer et al. (2015). The close binary sample consists of close binary systems with short orbital period of 30 days and less which have a solved orbits. Radial velocities are measured for the SPY sdB and sdO sample and the process is explained in detail in section 5. The kinematic analysis has been carried out in three different mass models of our Galaxy to study the impact of the chosen gravitational potential and the method for stellar population classification is adapted from Pauli et al. (2006). Both are explained in detail in section 4. The process for the kinematic analysis of this research is described in section 6 while all results are noted in section 7.

But first, the objects for this research are introduced. The evolution of hot subdwarfs and their charactersitcs are explained in section 2. The basic physics to carry out kinematic analysis are explained in section 3.

2 Hot Subdwarfs Type O and B

The categorization of subdwarfs derives from the group of hot stars accumulating below the main sequence stars in the Hertzsprung-Russell diagram (HRD). Main sequence stars like the Sun are called dwarf stars due to their small size compared to giants and supergiants, but subdwarf stars have radii typically ten times smaller than the sun.

2.1 Stellar Evolution

A star passes through various stages in its lifespan. While each of them has different characteristics all of them are summarized in the HRD. It is the most important tool in stellar astrophysics to classify and analyze different evolutionary stages of stars. As seen in figure 2 the HRD shows the relationship between a star's luminosity L and its effective temperature T_{eff}. Since the luminosity L is directly related to absolute magnitude M_{bol} and spectral types are based on effective temperature T_{eff} the HRD has different variants.

A star begins its life in the main sequence and stays at this stage for the longest time. It sustains its energy by burning hydrogen to helium in its core. How long a star stays in the main sequence strongly depends on its mass M. A star like the sun with $1\,\mathrm{M}_\odot$ stays for about 10^{10} years in this stage while a star with $15\,\mathrm{M}_\odot$ leaves the main sequence already after 10^7 years. As soon as the hydrogen resources in the core reach their end the envelope expands to form a red giant (RGB) and the star begins to burn hydrogen in a shell. If a star has enough mass to provide high temperature and pressure it sustains by fusioning higher elements. But if it can't its evolutionary path reaches its end.

Fusion is available when a star is massive enough. If a star has a lower mass than $0.45\,\mathrm{M}_\odot$ it won't reach the requirements for a more advanced fusion than H-burning. Therefore, it will continue burning hydrogen in its shell until the temperature drops and gravity exceeds the gas pressure contracting the star to a white dwarf.

A star with a mass larger than $0.45\,\mathrm{M}_\odot$ can ignite helium at the tip of the RGB.Its shell expands and burns hydrogen. The resulting helium core heats up and is stabilized by degenerate electron gas, which can't expand unlike ideal gas. Therefore, the produced heat is trapped resulting into more nuclear reactions and more heat is released until the helium flash. Finally the degeneracy of the electron gas is lifted at very high temperature. The star contracts and moves to the horizontal branch (HB) in the HRD, where helium is fusioned to carbon and oxygen, which lasts for about 100 million years.

With no more helium left in the core the only available helium is now in a shell below the hydrogen shell and the envelope expands to again form a red giant on the asymptotic giant branch (AGB). While the star is expanding it loses surface material creating a planetary nebula as a post-AGB star. The temperature is stable until all helium resources are used up, which causes the star to collapse into a white dwarf (WD) consisting of carbon and oxygen.

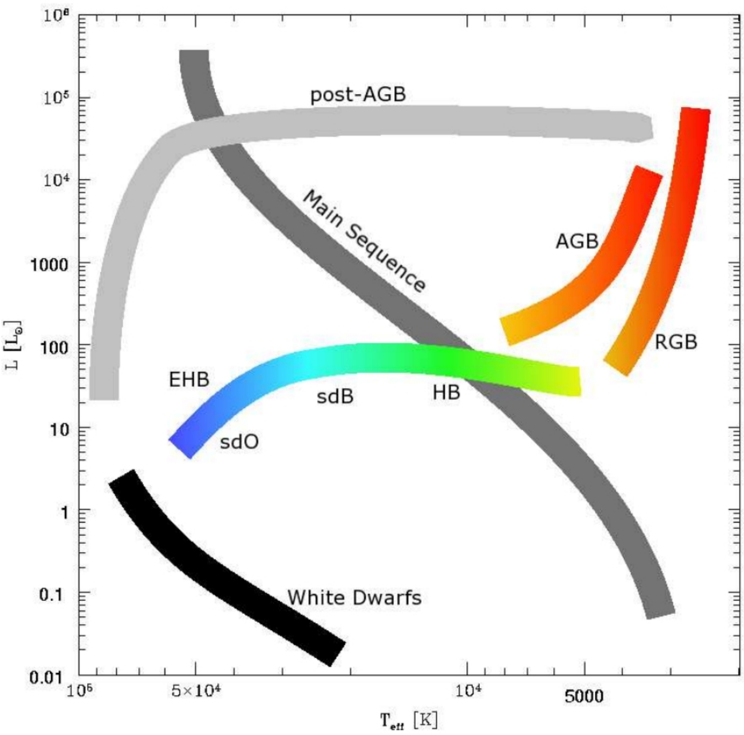

Figure 2: Schematic description of a HRD with marked position of the EHB (Hirsch, 2006)

2.2 Characteristics of sdO and sdB stars

The position of hot subdwarfs in the HRD is also called the extreme horizontal branch (EHB) which contains stars with low mass around 0.5 $M_\odot$ and luminosities of 10 to 100 times of $L_\odot$. Hot subdwarfs reach high effective temperatures T_{eff} of 20000 K for type B stars and more than 40000 K for type O stars.

EHB stars originate from RGB stars. However, EHB stars have an envelope mass smaller than 0.01 $M_\odot$ which can't sustain a burning hydrogen shell. Nevertheless, the helium flash occurs for all stars at a mass of 0.5 $M_\odot$. They move on the horizontal branch, but the additional mass of the shell defines the exact position. The low mass shell of EHB stars results into high surface temperature. Instead of proceeding their evolution on the RGB they evolve into white dwarfs after the helium flash.

The loss of almost all of the envelope mass can be explained in different ways. A single star near the tip of the RGB can lose its shell due to strong stellar wind. If two helium rich white dwarf merge due to energy loss caused by gravitational wave radiation, a new single star is created. The total mass needs to be above 0.46 $M_\odot$, which is the lower limit for helium fusion. Hot subdwarf of type B have a significant percentage of binary systems. Their origin can be described in the common-envelope process. If a red giant with a companion of unequal mass fills its Roche lobe, it will initiate an instable fast mass transfer to the companion. The additional material can't be accreted fast enough whereas the companion enters the shell of the red giant. This leads to friction, a loss in angular moment and a smaller orbit. As soon as the red giant ejects its shell a close binary system with short orbital period of less than 30 days is created.

3 Basic Physics for Kinematic Studies

Before any kinematic analysis may be carried basic astrometric data about the observed object are needed. In the case of stellar studies we are taking advantage of the gravitaional potential of our Galaxy. But to solve the equation of motion six basic variables of each star are required. Three of them determine its position in space and three are the corresponding velocity components.

3.1 Distance

There are different ways to determine the distance of a star and every method has its own benefit. The only direct measurement of the distance of a star is its trigonometric parallax. High precision data became available in April 2018 from the gaia mission. However, if the precision of a parallax is considered insufficient, the distance is calculated using methods of spectroscopy.

The annual parallax is the apparent shift in position of a nearby star most noticable in a half year difference. By taking advantage of two opposing positions of Earth looking at the same nearby star from different angles causes an apparent movement in contrast to the distant and set background.

If a star is located perpendicular to Earth's motion around the sun its parallactic path will be circular, but if it lies in the ecliptic plane its path will be a line. In general, though, we will observe an elliptical path. With trigonometry and making use of the small-angle approximation the small observed shifts are measured as parallax angles p. They are given in arcsecond (as) and can be transformed to distance d in parsec (pc).

$$d = \frac{1}{p}$$

A star's distance of 1pc indicates 1as for the parallax angle p. 1pc is equivalent to 3.09×10^{16} m or 206 264.8 AU or 3.26 ly. These observed shifts are easilier noticable the closer a star is. But unfortunately stars are often far away making it hard to observe the Earth reflex motion, which renders parallax measurements difficult for distant stars.

Indirect ways to calculate distances are methods of spectroscopy and photometry. Since no geometric or angular measurements are needed it is often used for distant objects where parallaxes aren't measurable. A downside is that more information is necessary to precisely determine the distance. The distance modulus is based on comparing a star's absolute visual magnitude M_V with its apparent visual magnitude m_V seen from earth.

$$m_V – M_V = 5\log(d) – 5$$

While the apparent visual magnitude m_V can be readily derived from photometry, the absolute visual magnitude M_V is harder to find. Since a star's brightness varies with distance the absolute visual magnitude M_V is defined by its brightness observed from a $10pc$ distance. It can be computed from its effective temperature T_{eff}, surface gravity $\log(g)$ and stellar mass M. The stellar radius R can be deprived from Newton's law of gravity where G is the gravitational constant.

$$g = \frac{GM}{R^2} \quad \Longleftrightarrow \quad R = \sqrt{\frac{GM}{g}}$$

The Stefan-Boltzman-Law defines luminosity L with the Stefan-Boltzmann constant σ which leads to the following using the computed stellar radius R.

$$L \;=\; 4\pi R^2\sigma T_{eff}^4 \;=\; 4\pi\frac{GM}{g}\sigma T_{eff}^4$$

This leads to the bolemetric magnitude M_{bol}, which describes the lumiosity of a stellar object across the whole electromagnetic spectrum while the visual magnitude M_V is restricted to the visual range only.

$$M_{bol} = -2.5\log(L) = -2.5\log(4\pi\frac{GM}{g}\sigma T_{eff}^4)$$

The absolute visual magnitude M_V and the bolemetric magnitude M_{bol} are related with the bolometric correction $B.C.$ as follwed.

$$M_V = M_{bol} + B.C.$$

3.2 Equatorial Coordinate System

The easiest way to pinpoint an object on the night sky provides the Equatorial Coordinate System (ECS) with the center of Earth in its origin. Because of its independence of the observer's time and location it is most suitable for cataloguing stars over years. It's similar to the Geographical Coordinate System used on Earth and indicates every star's position as a pair of right ascension α and declination δ.

The primary direction of the ECS is called right ascension α which is the celestial counterpart to terrestial latitude. By projecting Earth's equator on to the night sky the celestial equator is generated. Starting from the March equinox it measures the angular distance of an object eastwards along the celestial equator from the meridian. Right ascension α is measured in sideral hours, minutes and seconds where 24h marks a full circle around the globe. On the northern hemisphere the March equinox is also known as the vernal equinox and it marks one of two intersection of the celestial equator with the ecliptic. The other intersection is called September equinox or autumn equinox.

In analogy to the terrestial the latitude declination δ measures the angular distance of an object perpendicular to the celestial equator and is customarily measured in degree, minute and second. The North Celestial Pole has a declination of $+90°$ giving all points north of the celestial equator a positive declination and a negative value for all points south of it including the South Celestial Pole with a declination of $-90°$. Obviously, for the celestial equator is the declination $0°$.

Earth's axis is almost constant over the course of a year and therefore the position of the March equinox as well. But for longterm observations axial precession and nutation show their influence and shifting the ECS slightly every year. To maintain consistency in data all positions recorded need to be referred to an epoch. A commonly used epoch is J2000 referring to the sky of January 1st of the Julian year 2000 exactly on 12 noon Terrestrial Time.

In this thesis all Equatorial Coordinates are taken from the astronomical database SIMBAD (simbad.u-strasbg.fr/simbad/).

3.3 Radial Velocity

As a velocity component of an object radial velocity describes the motion along the line of sight. In astronomy it indicates how fast an observed object is moving away or towards Earth. Together with the transversal velocity component v_{tr} the total velocity v_{ges} of a star can be calculated

$$v_{ges} = \sqrt{v_{tr}^2 + v_{rad}^2}$$

The movement of an object emitting electromagnetic radiation relative to an observer causes a shift in its observed wavelengths, which is known as Doppler Shift. If it is moving away from the observer its spectrum is shifted to longer wavelength which is called red-shifted, but if it is moving towards the observer its spectrum is shifted to shorter wavelength which is called blue-shifted. The measured difference in wavelength $\Delta\lambda$ of a spectral line observed with respect to its rest wavelength λ_0 can be calculated as followed.

$$\frac{v}{c} = \frac{\Delta\lambda}{\lambda_0}$$

v is the speed of the observed object directed away from the observer and $c = 2.99792458 \times 10^8 \frac{m}{s}$ is the speed of light. In stellar astrophysics this non-relativistic formula is still accurate since even the fastest star known US708 doesn't exceed the speed limit of $0.01c$ for relativitic calculations. Since the Earth is rotating around the Sun an additional shift can be observed depending on Earth's orbit, that needs to be considered while determining radial velocities of stars. Therefore, the observational point of measurement is relocated at the mass center of our Solar System, which is a rather constant point throughout the years. This consideration is realized by the barycentric correction. All spectra taken from a telescope on Earth contain the same absorption lines imposed by the Earth atmosphere known as the telluric lines, which are mostly due to water vapour, ozone and other molecules.They are important tools to check the wavelength calibration. The date and time of the observation, the equatorial coordinates of the star for the standard epoch J2000.0 and the geographic position of the telescope are needed to compute the barycentric correction.

3.4 Proper Motion

Proper motions are the observed changes in the apparent places of an object as seen from the center of mass of our solar system. By comparing photographic sky images taken over years a small difference in position relative to the distant background may be noticed. In the equatorial coordinate system this two dimensional displacement is given in the direction of right ascension $\mu_\alpha cos(\delta)$ and declination μ_δ. Computing both values gives the total proper motion μ.

$$\mu = \sqrt{\mu_\alpha^2 cos^2(\delta) + \mu_\delta^2}$$

The correction term $cos(\delta)$ is necessary to describe the observed velocities in the direction of right ascension α and declination δ. A star's motion is measured in an orthogonal system using photographic plates. But since the night sky is a sphere and not a flat surface this correction is necessary. A star's transversal velocity component v_{tr} is computed from total proper motion μ and distance d. On average the proper motion of a star is larger for closer stars since their angular distance is more perceivable. However, if it also moves along the line of sight proper motion decreases. In this thesis all proper motions are taken from the Gaia Data Release 2.

3.5 The Galactic Coordinate System

All variables discussed are valid for an observer on Earth. If we want to study the structure of the Galaxy another coordinate system is more appropriate to specify position and movements of Galactic objects. The Galactic Coordinate System is a good choice for kinematic studies.

With Sagittaurus A* at its origin a cartesian coordinate system is drawn with one direction X pointed towards the sun, Y perpendicular to X in the Galactic plane and Z perpendicular to the Galactic plane.

The corresponding velocity components are the Galactic radial component U with positive value towards the center of the Galaxy, V as velocity component in direction of the Galactic rotation and a perpendiclar velocity component to the Galactic disk W, positive towards the North Galactic Pole.

The Sun has a distance of $8.4kpc$ from the Galactic centre and its motion relative to the local standard of rest (LSR) is $U_{\odot} = 11.1\frac{km}{s}$, $V_{\odot} = 12.24\frac{km}{s}$ and $W_{\odot} = 7.25\frac{km}{s}$. Important to note is the velocity component of the LSR $V_{LSR} = 242\frac{km}{s}$ (Irrgang et al., 2013).

4 Stellar Populations

The Galaxy hosts different stellar populations which have distinct kinematical properties. Stars from each class have similar traits and differ from other classes. Before talking about stellar populations the structure of our Galaxy has to be described. A lot of research on the gravitational potential of the Milky Way has been done, but there are different approaches to describe what has been observed. Three canonical mass models are commonly used to describe the gravitational potential of our Galaxy.

4.1 Structure of our Galaxy

Our Galaxy, the Milky Way, is a barred spiral galaxy. It consists of a bulge in the center with the bar, the Galactic disk including spiral arms which has a flat rotation curve and a halo all around it.

The size of the Galactic disk reaches from $30kpc$ to $50kpc$ in diameter depending on where to define the end of a thinning disk. The Galactic disk is often devided in two components called thin and thick disk. The thin disk has an average height of about $100 - 200pc$. It contains most stars of the Galaxy which are almost equally spread and star formation in the spiral arms which are areas of enhanced density. With about $8pc$ distance from the center, the Sun is part of the thin disk. The thick disk contains only a fraction of stars of the thin disk and is more extended with a scale of 1 kpc to 3 kpc.

The bulge is an almost spherical spatial extent. It's a very dense area and contains the Milky Way's bar. Tracking motions of the inner stars indicates the existence of a massive compact object within a faint radio source called Sagittaurus A* which is best described as a supermassive black hole.

Around the Galactic plane is a spherical shell called halo consisting of old stars, globular clusters and dark matter. With an estimated extend up to 200 kpc it encloses bulge and Galactic disk completely. It has a very low stellar density decreasing with a steep power law ($n \sim r^{-3.5}$) and doesn't have any interstellar gas which makes it the least populated part of the Galaxy.

4.2 Criteria for Star Populations

One aim of kinematic studies is to determine what kind of population stars observed belong to. By looking at a their orbital characteristics they can be assigned to either the thin disk population, the thick disk population or the halo population, which each corresponds to a certain region in the Galaxy.

Pauli (2003) developed a method to distinguish star membership in a process of elimination which will be used in a slightly different form later on in this theses. According to their method every star is classified in three different categories which are its position in the U-V-diagram, its position in the J_Z-e-diagram and its orbital behavior in the ρ-Z-diagram. Each of them has a classification variable assigned to which are described as c_{UV}, c_{J_ze} and c_{orb}. Pauli (2003) starts to look out for halo stars first. By investigating all three criteria of a star each classification variable is assigned to a value of $+1$ if the stars shows characteristics of a halo population in its respective category and a value of -1 if it doesn't. In the end all variables are sumed up to the total factor c.

$$c = c_{UV} + c_{J_ze} + c_{orb}$$

All stars with $c \geq 1$ are categorized as halo population whereas stars with $c < 1$ belong either to thin or thick disk population. In order to seperate the thin disk population from the thick disk population Pauli (2003) use the same procedure. Instead of focusing at halo characteristics, thick disk characteristics are considered. Each variable c_{UV}, c_{J_ze} and c_{orb} gets a value of ± 1 depending if it shows thick disk

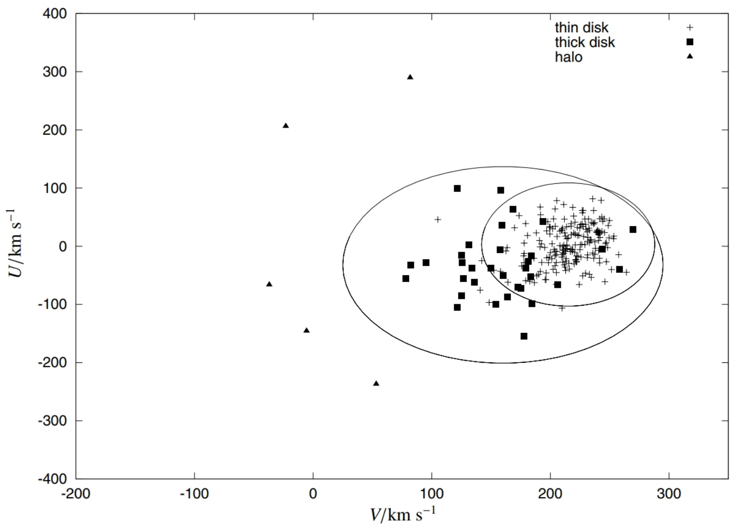

Figure 3: $U - V$ diagram for main sequence stars with $3\sigma_{thin}$- and $3\sigma_{thick}$ contours(Pauli et al., 2006)

characteristics. Summing up all variables to obtain the total factor c leads the final characterization. Stars with $c \geq 1$ belong to thick disk population and stars with $c < 1$ are part of the thin disk population.

4.2.1 $U - V$ Velocity Diagram

The velocity diagram is a popular tool to get a quick glance about the velocity distribution. U and V are the velocity components in the Galactic plane. For the thin and the thick disk stars the mean values and the standard deviation have been calculated as followed (Pauli, 2003).

- Thin disk: $U_0 = 3\,\frac{\mathrm{km}}{\mathrm{s}}, \sigma_U = 105\,\frac{\mathrm{km}}{\mathrm{s}}, V_0 = 215\,\frac{\mathrm{km}}{\mathrm{s}}, \sigma_V = 72\,\frac{\mathrm{km}}{\mathrm{s}}$
- Thick disk: $U_0 = -32\,\frac{\mathrm{km}}{\mathrm{s}}, \sigma_U = 168\,\frac{\mathrm{km}}{\mathrm{s}}, V_0 = 160\,\frac{\mathrm{km}}{\mathrm{s}}, \sigma_V = 135\,\frac{\mathrm{km}}{\mathrm{s}}$

Figure 3 shows the calibration sample of main sequence stars used by Pauli et al. (2006). Most thin disk stars are within the $3\sigma_{thin}-$limit of the thin disk and all thick disk stars lie within their $3\sigma_{thick}-$limit. Halo stars are outside of both 3σ-regions.

4.2.2 $J_Z - e$ Eccentricity Diagram

Velocity diagrams give a hint about a star's population membership, but it can't be used alone. The eccentricity e of an orbit is a good indicator for memberships when paired with the angular momentum J_Z in Z direction.

Figure 4 shows the calibration sample of main sequence stars used by Pauli et al. (2006) which indicates that thin disk stars are located in a low eccentricity area with a high angular momentum J_Z called Region A. Thick disk stars mostly have a higher eccentricity e than thin disk stars, but have a lower angular momentum J_Z. For thick disk stars Region B is marked as a parallelogram in the $J_Z - e$-diagram with $J_{Z,min} = 1100\,\frac{\mathrm{kpc\,km}}{\mathrm{s}}, J_{Z,max} = 1800\,\frac{\mathrm{kpc\,km}}{\mathrm{s}}$ at $e_{min} = 0.27$ and $J_{Z,min} = 400\,\frac{\mathrm{kpc\,km}}{\mathrm{s}}, J_{Z,max} = 1100\,\frac{\mathrm{kpc\,km}}{\mathrm{s}}$ at $e_{max} = 0.7$. Halo stars are commonly found in Region C which is characterized by high eccentricity e and low angular momentum L_Z.

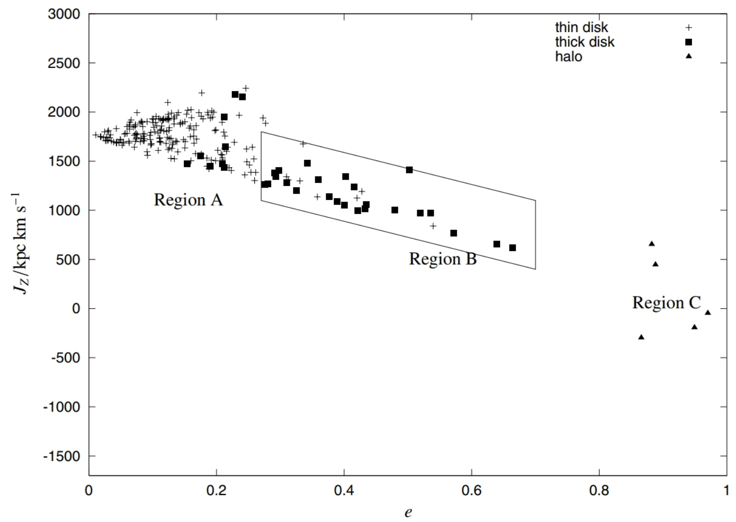

Figure 4: $J_Z - e$ diagram for main sequence stars (Pauli et al., 2006)

4.2.3 $\rho - z$ Meridional Diagram

The last tool to fully comprehend the orbital behavior of a star is the meridional diagram. It plots a star's position in z direction as a funktion depending on its radial position $\rho = \sqrt{x^2 + y^2}$. Therefore it is a projection of the orbit onto the $\rho - z$ plane. The categorization in different star population is given by the extent in z direction of each orbit. Thin disk stars have a very plane orbit with almost no extend in z direction as it is shown in Figure 5. The chosen limit for this diagram is $z = \pm 1$ kpc.

The thick disk population encompasses the thin disk population and therefore has a significant extent in the z direction up to 3 kpc. Figure 6 is an example of a typical meridional plot of a thick disk star. Every star that exceeds this limit is identified as a halo star. Often their orbits are very irregular, reach the outer parts of our Galaxy or have a chaotic nature as shown in Figure 7.

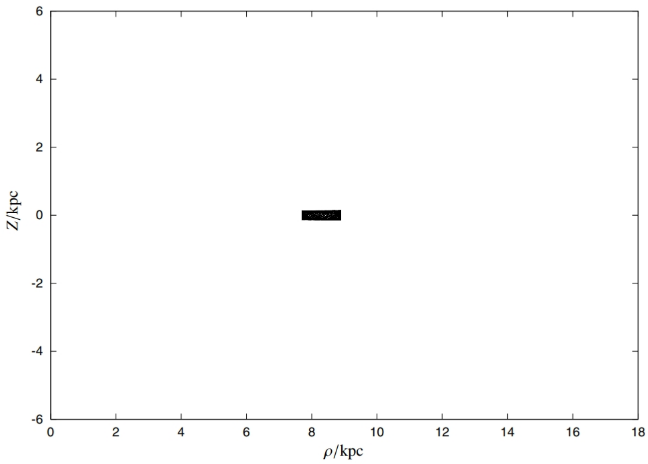

Figure 5: White dwarf WD0310-688 with a thin disk orbit (Pauli et al., 2006)

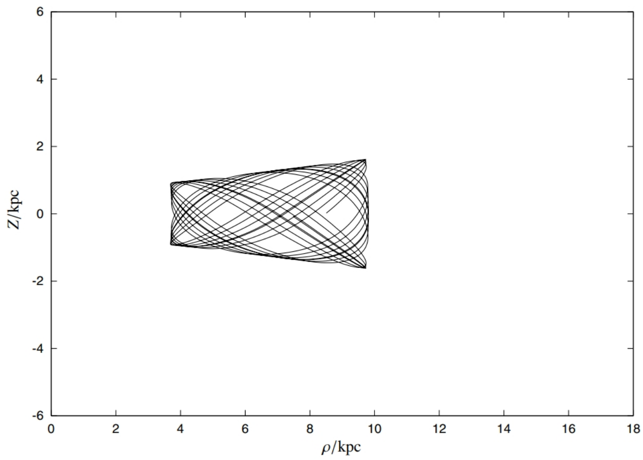

Figure 6: White dwarf WD1013-010 with a thick disk orbit (Pauli et al., 2006)

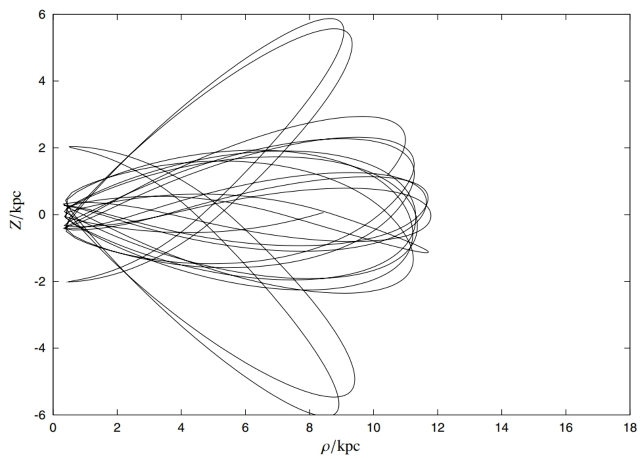

Figure 7: White dwarf HS 1527+0614 with a chaotic halo orbit (Pauli et al., 2006)

4.3 Mass Models of our Galaxy

When all components of a stellar motion equation are known a star's orbit can be computed using the gravitational potential of the Galaxy $\Phi(r,z)$ where r und z are two components of the cylindric coordinate system. It is a sum of potentials of the bulge $\Phi_b(r,z)$, the disk $\Phi_d(r,z)$ and the spherical dark matter halo $\Phi_h(r,z)$.

$$\Phi(r,z) = \Phi_b(r,z) + \Phi_d(r,z) + \Phi_h(r,z)$$

However, the Milky Way's mass distribution is not well known, especially the dark matter halo is poorly known. Therefore, three different and widely used model potentials are considered. From improved observational contraints, Irrgang et al. (2013) recently updated them. All three models share the same gravitational potential for the bulge $\Phi_b(r,z)$ and the disk $\Phi_d(r,z)$.

$$\Phi_b(R) = -\frac{M_b}{\sqrt{R^2 + b_b^2}}$$

$$\Phi_d(r,z) = -\frac{M_d}{\sqrt{r^2 + \left(a_d + \sqrt{z^2 + b_d^2}\right)^2}}$$

The parameters a and b are scale lengths and $M_{i,d}$ describe the mass of the coresponding part of the Galaxy.

Model I is a revision of the Allen & Santillan (1991) potential. It focuses on an asymptotical behavior for M_h for large R which is motivated by the observed flat rotation curve. The cut-off paramter Λ is intruduced to prevent an unphysical infinite halo mass and the free parameter γ reduces complexity, avoids singularities and matches best to the observations for $\gamma = 2$. For $\Lambda = 100\,\text{kpc}$ and $\gamma = 2.02$ this potential is equivalent to the original Allen & Santillan (1991) potential. The resulting total mass of the Galaxy is $M_{total} = 1.9^{+2.4}_{-0.8} \times 10^{12} M_\odot$ and the mass within 50kpc is $M_{R<50\,\text{kpc}} = 5.1^{+3.3}_{-0.4} \times 10^{11} M_\odot$, which defines the escape velocity $v_{esc}(r,z) = \sqrt{-2\Phi(r,z)}$ at the Sun's position to about $v_{esc} = 616\ \frac{\text{km}}{\text{s}}$.

$$\Phi_{h,I}(r,z) = \begin{cases} \frac{M_h}{a_h}\left(\frac{1}{(\gamma - a)} \ln\left(\frac{1+\left(\frac{R}{a_h}\right)^{\gamma-1}}{a+\left(\frac{\Lambda}{a_h}\right)^{\gamma-1}}\right) - \frac{\left(\frac{\Lambda}{a_h}\right)^{\gamma-1}}{1+\left(\frac{\Lambda}{a_h}\right)^{\gamma-1}}\right) & \text{if } R < \Lambda \\ -\frac{M_h}{R}\frac{\left(\frac{\Lambda}{a_h}\right)^{\gamma}}{1+\left(\frac{\Lambda}{a_h}\right)^{\gamma-1}} & \text{if } R \geq \Lambda \end{cases}$$

In Model II the halo is replaced with a flat rotational curve model. The resulting gravitational potential has a flat rotational curve in the inner parts of the Galaxy and it doesn't need a cut-off parameter to prevent an unphysical infinite halo. However, the scale parameter a_h is limited to 200kpc which results to an upper limit of the total mass $M_{total} = 1.7^{+0.2}_{-0.5} \times 10^{12} M_\odot$ and a mass within 50kpc of $M_{R<50\,\text{kpc}} = 4.6 \pm 0.3 \times 10^{11} M_\odot$ resulting in a local escape velocity v_{esc} of $576\ \frac{\text{km}}{\text{s}}$. This implies a lower gravitational potential $\Phi(r,z)$ and lower mass M.

$$\Phi_{h,II}(R) = -\frac{M_h}{a_h} \ln\left(\frac{\sqrt{R^2 + a_h^2} + a_h}{R}\right)$$

In Model III the gravitational potential of the halo $\Phi_{h,III}(R)$ is based on the universal density profile of dark matter halos. Characteristic for this model is that the halo mass M_h diverges logarithmically for $R \longrightarrow \infty$. Compared to the previous models Model III has a rising rotational curve outside of the Sun's orbit, peaking at 82kpc and decreasing beyond. This approach results into a logarithmical infinite total mass M_{total} and a mass withing 50kpc $M_{R<50\,\text{kpc}}$ that exceeds the mass of other models by the factor

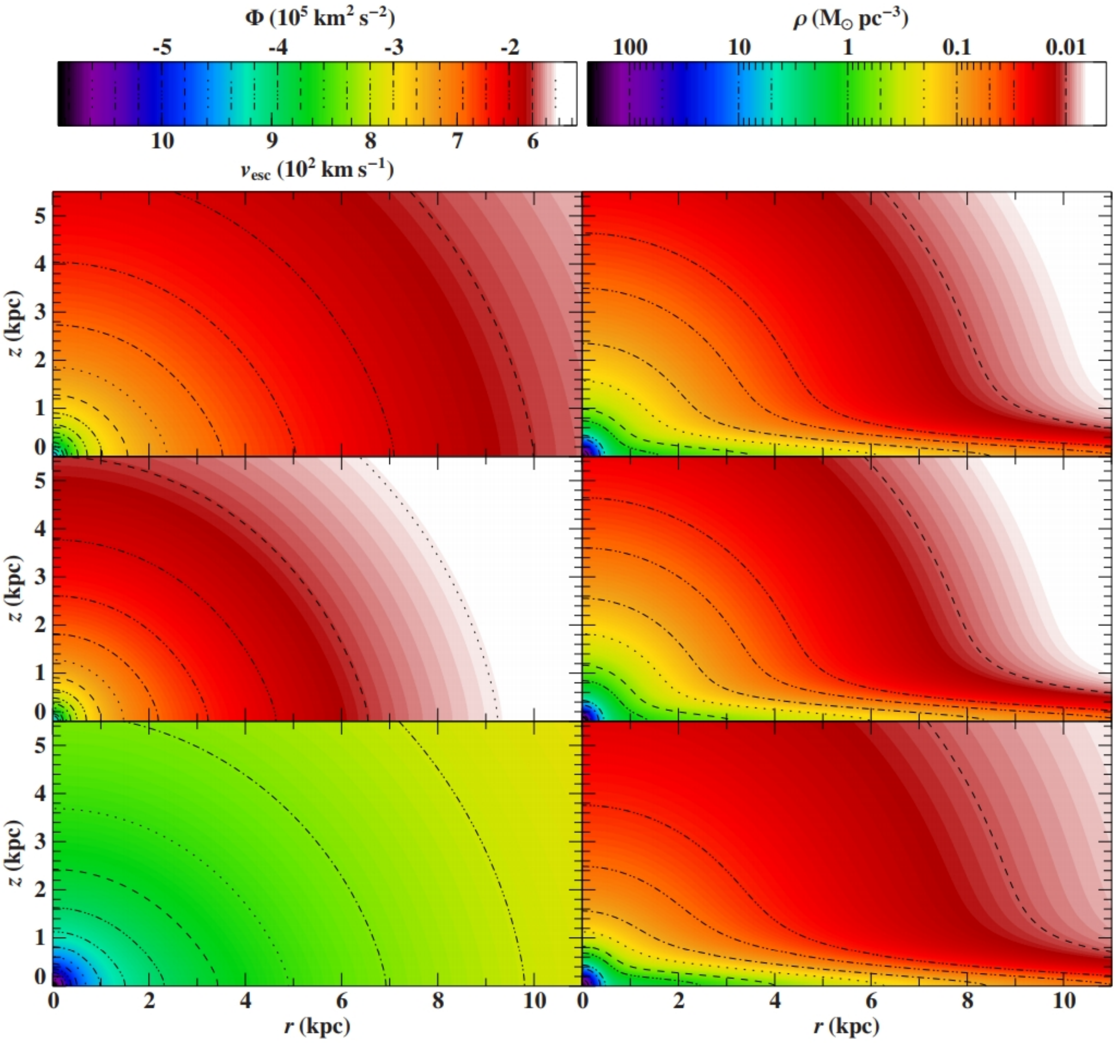

Figure 8: Gravitational potential $\Phi(r, z)$, escape velocity $v_{esc}(r, z)$ and total mass density $\rho(r, z)$ for the best fit parameters of Model I (upper panel), Model II (middle panel) and Model III (lower panel) (Irrgang et al., 2013)

1.5. Alternatively the total mass can be described as the mass M_{200} within a sphere of radius r_{200}, which is defined by the mean interior density fo 200 times the critical value for a closed universe. This leads to the radius $r_{200} = 319^{+61}_{-58}\,\mathrm{kpc}$, the mass $M_{200} = 4.0^{+1.2}_{-1.8} \times 10^{12} M_\odot$ and the local escape velocity v_{esc} of $812\,\frac{\mathrm{km}}{\mathrm{s}}$.

$$\Phi_{h,III}(R) = -\frac{M_h}{R} \ln\left(1 + \frac{R}{a_h}\right)$$

5 Determining Radial Velocities

The radial velocity is one basic component of a star's motion needed to obtain its orbit. We can easily determine it by investigating its spectrum. Making use of the Doppler effect and adjusting small corrections radial velocity can be precisely determined.

5.1 The SPY Project

All analyzed spectra are taken from the SPY Sample. In the early 2000s a large spectroscopic survey of more than 1000 white dwarfs and hot subdwarfs was carried out to find radial velocity variables indicative of binarity. SPY is short for the ESO Supernovae Type Ia Progenitor Survey and sets its focus on the search for binary white dwarfs as progenitors of type Ia supernovae (Napiwotzki et al., 2003), to test a popular scenario for a supernova explosion via the merging of two close white dwarfs with very short orbital period.

All stars were observed with the UV-Visual Echelle Spectrograph (UVES) at the UT2 telescope (Kueyen) of the ESO Very Large Telescope which can provide high resolution of 110000. Using a wide slit to reduce slit losses results in a resolution of 18500 for this observation. All spectra have nearly complete coverage from $3200\AA$ to $6650\AA$ with only two small gaps of about $80\AA$ width at $4580\AA$ and $5640\AA$. Each exposure time varies from 5 min to 10 min depending on the brightness of the star observed. This program took advantage of observing conditions which were not suitable for other programs like full moon or partly clouded weather which leads to an average signal to noise ratio per binned pixel ($0.03\AA$) of 15 or higher. Furthermore all stars have been observed at least two times with minimum 24 h in between, but mostly it's a few days or months difference in time.

5.2 The Close Binary Sample

Binary systems must be approached differently than single stars. Due to the two mass system the measured radial velocity v_{rad} needs to be interpreted as a computed velocity made out of the system velocity γ and the amplitudal velocity K. Longterm observations are required to recognize the recurring pattern in velocity and to determine both velocity components as precisely as possible. Kupfer et al. (2015) investigated close binary systems with short orbital period of less than 30 days. They determined new data for twelve new systems and also gathered astronometric data of 142 sdB close binary systems which have been rinvestigated since 1986.

There is a small overlap with stars from the SPY sample. For stellar population classification this sample provides system velocity γ. Therefore, there is no need for additional RV measurements.

5.3 Spectra Analysis

A total of 121 sdB and sdO stars taken from Lisker et al. (2005) and Stroeer et al. (2007) were in focus for spectra analysis. Some were already recognized as a close binary system by Kupfer et al. (2015) and therefore have a known system velocities γ. Due to the nature of binary systems with short periods observed radial velocities won't give a sufficient representation of the system's movement. In a binary system both stars circle around their center of mass which causes a regular change in their measured radial velocities. Only a long observation over multiple periods results in a reliable system velocity γ. Stars that are part of the SPY sample and the close binary sample are shows in Table 1.

Binary systems with a cool companion are known for their long periods which can extend to several years with RV semi-amplitudes of few km/s only. Therefore, all measured radial velocites of binary

Table 1: Close binaries of the SPY sample with solved system velocities γ taken from Kupfer et al. (2015)

star	**type**	$\gamma[\frac{km}{s}]$	$\sigma_\gamma[\frac{km}{s}]$
EGB 5	SdB	68.5	0.7
HE 0230-4323	SdB	16.6	1.0
HE 0532-4503	SdB	8.5	0.1
HE 0929-0424	SdB	41.4	1.0
HE 1047-0436	SdB	25.0	3.0
HE 1421-1206	SdB	-86.2	1.1
HE 1448-0510	SdB	-45.5	0.8
HE 2135-3749	SdB	45.0	0.5
HE 2150-0238	SdB	-32.5	0.9
HS 2043+0615	SdB	-43.5	3.4
HS 2359+1942	SdB	-96.1	6.0
GD 687	SdB	32.3	3.0
PHL 861	SdB	-26.5	0.4
HE 1059-2735	SdO	-44.7	0.6
HE 1115-0631	SdO	87.1	1.3
HE 1130-0620	SdO	8.3	2.2
HE 1318-2111	SdO	48.5	1.2

systems with a cool companion can be considered reliable with an additional systematic error. Radial velocities v_{rad} are remeasured for all stars without known system velocity γ.

As mentioned above the spectra ranged from $3200\mathring{A}$ to $6650\mathring{A}$ and came in three parts due to the three CCD channels inside UVES. After merging them together they were ready for examination. The radial velocities v_{rad} were measured by fitting mathematical functions to absorption lines of hydrogen, helium and metals if present using the program SPAS v0.9.22 made by Heiko A. Hirsch. Hydrogen Balmer lines are broad and easy to find, but they come with the highest inaccuracy of all. Helium lines are narrower than hydrogen lines but are only present if helium is sufficiently abundant. Metal lines are the sharpest of all lines and therefore allow for the highest precision if present, but due to their narrow nature weak metal lines are hard to find at high noise levels. Since some spectra had a very low signal to noise ratio S/N of 10 and below metal lines weren't always available. Chosing the most reliable lines depending on their accuracy and presence was individually determined, but it was always aimed to fit a minimum of 10 lines in total. A selection of ions were used for velocity determination including hydrogen, helium I and II, carbon II, III and IV, nitrogen II, III and IV, oxygen II, III and IV, magnesium I, II, III and IV, aluminium III, silicon II, III and IV and sulfur II and III.

All calculated radial velocities v_{rad} are barycentric corrected with MIDAS version 12FEBpl1.3 provided by ESO. On average two spectra are available for each star resulting in different radial velocities $v_{rad,i}$ and errors σ_i, which allows us to judge wheather the star is RV variable or not. Therefore, a weighted mean $< v_{rad} >$ for each star was computed as followed.

$$< v_{rad} >= \frac{1}{n}\sum_{i=1}^{n} v_{rad,i} + \frac{1}{n^2}\sum_{i=1}^{n}\sigma_i^2$$

The total error σ_v is computed accordingly.

$$\overline{v}_{rad} = \frac{1}{n}\sum_{n=1}^{n} v_{rad,i}$$

$$\sigma_v = \sqrt{\left(\frac{\partial \overline{v}_{rad}}{\partial v_i}\right)^2 \sigma_i^2}$$

All stars known having a cool companion gain an additional systematic uncertainty of $+5\frac{km}{s}$. If a star is identified as a close binary a conservative estimate of $+100\frac{km}{s}$ is added to σ_v. Furthermore there are stars not known to be close binaries, but with a distinct spread in their radial velocities $v_{rad,i}$ of more than 2σ. These measurements can't be explained by a single star's movement and therefore a systematic error of $+100\frac{km}{s}$ is added to their computed error σ_v as a possible candidate for a radial velocity variable star.

6 Kinematic Analysis

6.1 Gaia Data

The space observatory Gaia located in the second Lagrangian point is a spacecraft designed to gather astrometric, photometric and spectroscopic data of stars with outstanding precision. Over the years it repeatedly executes sky surveys to increase accuracy until the end of its mission. On April 25th 2018 the second Gaia Data Release provided the remaining data needed to calculate a stellar orbit including proper motions and parallaxes. Since the Gaia mission is an ongoing project all data received are still a work in progress and will gain precision while observing. All proper motions came with an astonishing small error, but parallax measurements were mixed in quality. Gaia provided an insufficient parallax with errors of 20 % or more for about 10 % of the analyzed sample. Therefore, a spectroscopic analysis of these stars was necessary to gain distance measurements.

6.2 Population Classification

After gathering all stellar data including coordinates, proper motion components, parallax or distance, radial or system velocity and parallax correlations the orbit of each star was calculated. With 2000 Myr in advance and 10000 Monte Carlo runs error propagation by MC simulations the given errors are in the 1σ limit. All calculations are based on three different mass models which have been discussed in chapter 4.3. The computed 3D information about Galactic position and velocites is given for the Galactic Coordinate System.However, all velocity components are given in direction of each cartesian axis v_X, v_Y and v_Z and need to be transformed into the velocity components U and V for further analysis.

$$U = \frac{x\,v_X + y\,v_Y}{\sqrt{x^2+y^2}} \qquad V = \frac{y\,v_X - x\,v_Y}{\sqrt{x^2+y^2}}$$

In the $U-V$ velocity diagram stars have been categorized in thin disk, thick disk and halo population according to the criteria discussed in chapter 4.2.1. The errors in its velocity components σ_V and σ_U have been considered by checking the respective criteria for the corners of the error rectangle $(V \pm \sigma_V, U \pm \sigma_U)$.

If at least one out of four corners of the error box is inside the $3\sigma_{thin}$ region a star is classified as a member of the thin disk population. If no corner is inside the $3\sigma_{thin}$ region, but at least one corner is inside the $3\sigma_{thick}$ region, the star is classified as part of the thick disk. For all other cases the star is classified as a halo star.

Further parameters of each orbit have been calculated such as perigalactic distance R_{min}, apogalactic distance R_{max}, the total energy E and the angular momentum J_Z. The eccentricity e can be computed as followed.

$$e = \frac{R_{max} - R_{min}}{R_{max} + R_{min}}$$

To determine stellar memberships in the $e - J_Z$ diagram the criteria explained in chapter 4.2.2 have been applied combined with the method of the error rectangle $(e \pm \sigma_e, J_Z \pm \sigma_{J_Z})$. Therefore a star is identified as a member of the thin disk population if all four corners are inside Region A which is defined as above the line $J_Z = \frac{400-1100}{0.7-0.27}\, e\, \frac{\mathrm{kpc\,km}}{\mathrm{s}}$, smaller than $e = 0.3$ and not inside the parallelogram for thick disk population is. If a minimum of one corner is outside of Region A or B the star is classified as halo candidate. In all other cases the star is identified as a thick disk member.

For the meridional plots all stars have been judged according to the criteria in chapter 4.2.3. Similar to the method of Pauli (2003) a stars is defined as part of either thin disk, thick disk or halo population by its resulting categorizations of each discussed diagram. The results of the $U - V$ velocity diagram, the $e - J_Z$ eccentricity diagram and the $\rho - z$ meridional diagram are equally weighted. If a star is categorized as a halo candidate in two or more diagrams, it is finally assigned to the halo population. If a star has two or more criteria for the thin disk membership, it is identified as a member of the thin disk population. For all other cases the star is categorized as part of the thick disk.

The kinematic parameters U, V and J_Z can be derived from the present position, the distance d, the proper motion μ and the radial velocity v_{rad}. The eccentricty e is derived from the orbit of the object.

7 Discussion

In this section all results will be discussed starting with the measured radial velocities and comparing them with published measurements. The following discussion will be about kinematics, which depend on the choice of the gravitational potential of our Galaxy. Therefore, the impact of the choice of the Galactic mass model is discussed before going into detailed analytics of the SPY sdB and sdO sample and the close binary sample.

7.1 Radial Velocities

All but one known close binary system have a significant spread in their measured radial velocities v_{rad} of 2σ and more. Only EGB5 can not be confirmed to be a close binary system from the SPY spectra only. However, Kupfer et al. (2015) listed this star as a low amplitude RV variable ($K = 16.1$ km/s) of relatively long period (16,5 days). In the sdB sample the percentage of close binary systems is 14.7%, whereas the sdO sample holds only 7.3%.

Most binary systems with a cool companion have radial velocities v_{rad} that could originate from a single star system, which are barely within the 2σ limit. This supports the idea of long orbital periods for binaries with a cool companion. The only outlier is HS2043+0615 with a difference in radial velocities Δv_{rad} of $80\frac{km}{s}$. 24.0% of the sdB sample are binary systems with a cool companion. On the other hand only one system like this can be found in the sdO sample which makes 2.4% of the total sample.

Table 2: New RV variable stars in the SPY sample with v_{rad} given in $\frac{km}{s}$

star	**sample**	$v_{rad,1}$	$v_{rad,2}$
HE0016+0044	sdB	30.012±1.186	22.971±1.012
HE0207+0030	sdB	61.204±3.564	-24.410±5.876
WD2020-253	sdO	129.055±0.996	120.386±0.842
PG0026+136	sdO	8.477±3.670	20.337±3.691

A total of 4 stars show a significant spread in their radial velocity v_{rad} that can't originate from a single star hinting to be radial velocity variable systems (RV variable). Table 2 shows stars of the sdB and sdO sample and their radial velocities v_{rad} with yet undetected binarity.

Maxted et al. (2001) researched a different sample of EHB stars which consists to 58,3% of close binaries. Compared to the SPY sample the percentage is 27,6%. Napiwotzki et al. (2004) investigated the SPY sdB and sdO sample as welll and detected 18 (39%) close binaries in the sdB sample and 1 (4%) in the sdO sample. The percentage of close binaries and RV variable stars in this research is at 14.67% for sdB stars, while the sdO sample consists to 7,3% of close binaries and RV variable stars.

Martin et al. (2017) investigated ten close binary systems which are also part of the SPY sample. The measured radial velocities v_{rad} are within the 2σ limit of this research.

7.2 Impact of the Chosen Galactic Mass Model

The kinematic analysis has been applied on all stars in three different mass models. The first result to mention is that the membership classification turns out to be nearly independent from the chosen mass model. A total of 233 stars from both SPY sample and the sample of binary sdBs have been categorized using to the method of elimination explained in section 4.2. The stellar membership is based on three different values given for each diagram which makes a total of $3 \times 233 = 699$ categorization in one model. When searching for discrepancies in the categorization results it becomes clear that eleven stars have different classification values for different mass models, but in only five cases these are sufficient to identify a star as part of a different membership as shown in table 3.

Table 3: Hot subdwarfs classified in different star populations depending on the mass model used

star	**Model I**	**Model II**	**Model III**
TonS137	thin	thick	thick
PG0958-073	thin	thin	thick
KIC10553698	halo	halo	thick
GD617	halo	halo	thick
EC13332-1424	halo	halo	thin

Table 3 shows the distribution of classification. The differences exist due to one classification value out of three being classified in a different population. If the other two values can not classify the star clearly in one stellar population, the third value will determine the overall classification for this star. When looking at the diagrams for classification it is clear that the star won't change dramatically its position. When set in a different gravitational potential the position in these diagrams slightly shifts. However if a star is close to a border for another population this shift determines a different classification for this star.

Overall there is no significant trend noticeable and the discrepancies per stellar classification is 2.1 % in regards of the chosen mass model. Therefore all further discussions focus on model I which is of intermediate mass between model II and III.

7.3 Kinematic Results

The results of the kinematic analysis for each sample are discussed in each subsection. According to the categorization method of Pauli et al. (2006), which is discussed in section 4.2, all stars have been categorized. As seen in figure 9-11 tree stars have been correctly identified as a member of each stellar population according to the $\rho - Z$ diagram.

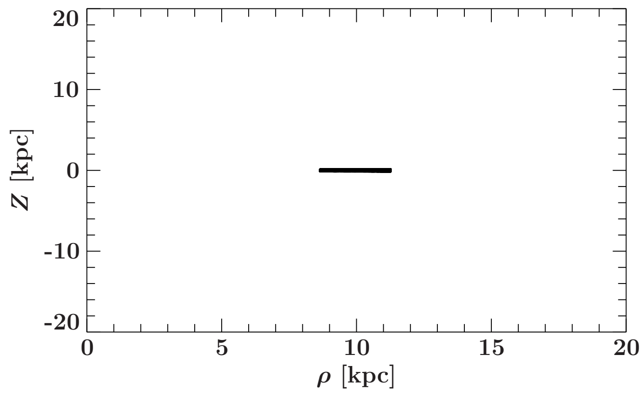

Figure 9: HZ1 identified as a thin disk star

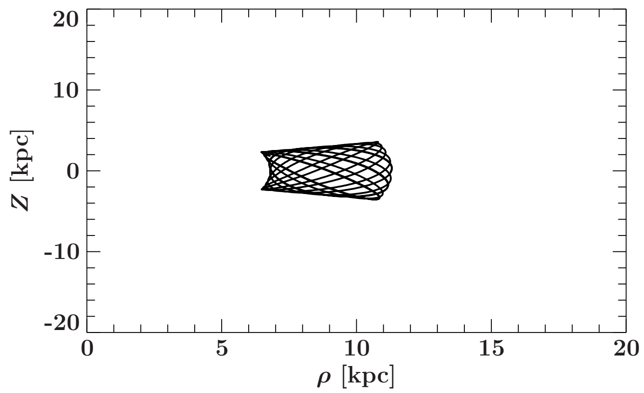

Figure 10: HS1536+0944 identified as a thick disk star

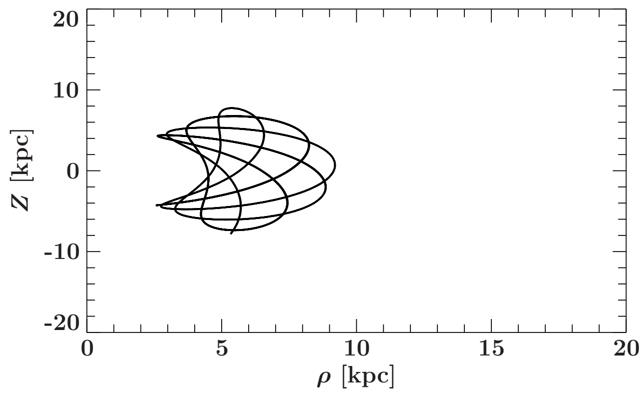

Figure 11: HE0136-2758 identified as a halo star

Table 4: Charakterization values for halo and thick disk members of the close binary sample in Model I

star	$\rho - z$	$U - V$	$e - J_Z$	**Model I**
J002323-002953	halo	halo	halo	halo
J102151+301011	halo	thick	halo	halo
J152222-013018	halo	halo	halo	halo
KIC10553698	halo	halo	halo	halo
Feige48	thick	thin	thick	thick
HE1115-0631	thick	thin	thin	thick
HE1414-0309	halo	thick	thick	thick
HS1741+2133	thin	thick	thick	thick
J082332+113641	thick	thin	halo	thick
J083006+475150	thick	thin	halo	thick
J095101+034757	halo	thick	thick	thick
J113840-003531	thick	thick	thick	thick
J134632+281722	thick	thin	thick	thick
J150513+110836	halo	thick	thick	thick
PB5333	thin	thick	thick	thick
PG0918+029	thin	thick	thick	thick
PG0941+280	thin	thick	thick	thick
PG1000+408	thick	thin	thick	thick
PG1519+640	thick	halo	thin	thick
PHL861	thick	thick	thick	thick

7.3.1 The Close Binary Sample

Overall 133 stars with sufficient information for analysis are part of this sample (Kupfer et al., 2015). The calculations show that five are halo candidates, which makes 3.8 % of the total sample. 16 stars belong to the thick disk, which is 12.0 %, but the majority of 84.2 % are thin disk stars. Table 4 displays the characterization values for all halo and thick disk members in Model I.

Figure 12 shows the $U - V$ and the $e - J_Z$ diagram for all stars of the close binary sample. The error bars are small thanks to the solved system velocities. The only star with a clear retrograde orbit is J152222-013018.

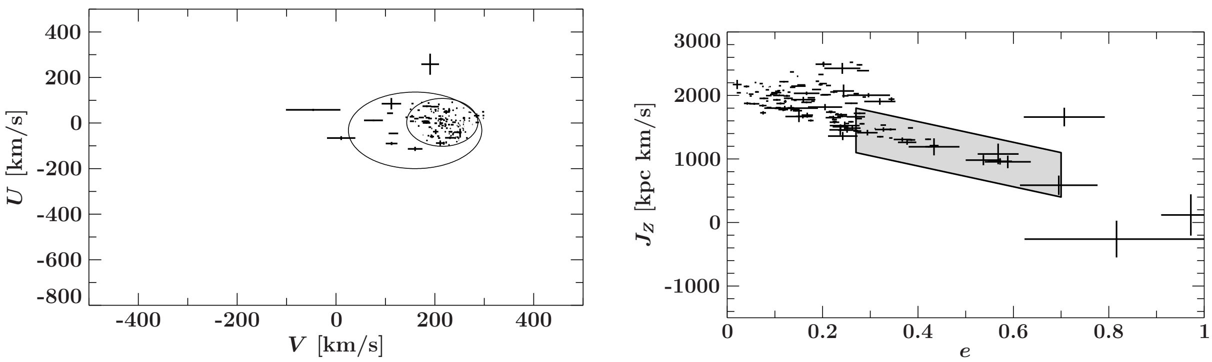

Figure 12: $U - V$ and $e - J_Z$ diagrams for the close binary sample in Model I

Table 5: Charakterization values for halo and thick disk members of the SPY sdB sample in Model I

star	$\rho - z$	$U - V$	$e - J_Z$	**Model I**
GD617	halo	thick	halo	halo
HE 0136-2758	halo	halo	halo	halo
HE 0151-3919	halo	halo	halo	halo
HE 0415-2417	halo	halo	halo	halo
HE 1419-1205	halo	halo	halo	halo
HS 1536+0944	halo	halo	halo	halo
TON S155	halo	halo	halo	halo
GD1237	halo	thick	thick	thick
HE0007-221	thick	halo	thin	thick
HE0019-5545	thick	thick	thick	thick
HE1415-0309	halo	thick	thick	thick
HE1422-1851	halo	thick	thick	thick
HE1459-0234	thick	thin	thick	thick
HE2151-1001	halo	thick	thick	thick
HE2237+0150	thick	thin	thick	thick
HE2238-1455	halo	thick	thick	thick
HE2322-4559	halo	thin	thick	thick
HE2349-3135	halo	thin	thick	thick
HS1530+0542	thick	thick	thick	thick
PG1549-001	thick	thin	thick	thick
PG2122+157	halo	thin	thick	thick
PHL861	thick	thick	thick	thick

7.3.2 The SPY Sample

The SPY sample contains hot subdwarfs of type O and B. There is an overlap with the close binary sample made out of twelve sdB and four sdO stars. Despite these 16 objects no other star has a solved system velocity γ and all radial velocities v_{rad} have been calculated as explained in section 5. Some stars have been reported as close single-lined binaries or as a system with a cool companion and some stars show hints to have yet unknown variable radial velocities v_{rad}. The distribution of binary sdB and sdO stars are discussed individually.

According to the calculations the sdB sample has 7 halo candidates which are 9.3 % of the sample, 15 thick disk stars which are about 20.0 % and it consists to 70.7 % of thin disk members. The distribution of binary systems can be taken from table 6. The total percentage of single stars in the sdB sample is 58.7 %. Binaries with a cool companion make up 24.0 % of the total sample. The count for close binary system is at 14.7 % including the new RV variable candidates. All characterization values of halo candidates and thick disk members of the SPY sdB sample are listen in table 5. The sdB sample has a couple of stars that reach in the negative region for U, but the ones with a clear retrograde orbit are HE0136-2758, HE2218-2026 and HS1536+0944.

Table 6: Population distribution of binary systems in the sdB sample for Model I

sdB star	**halo**	**thick**	**thin**	**all**
single stars	5	11	28	44
cool companion	2	2	14	18
close binary	0	2	9	11
rv variable	0	0	2	2
all	7	15	53	75

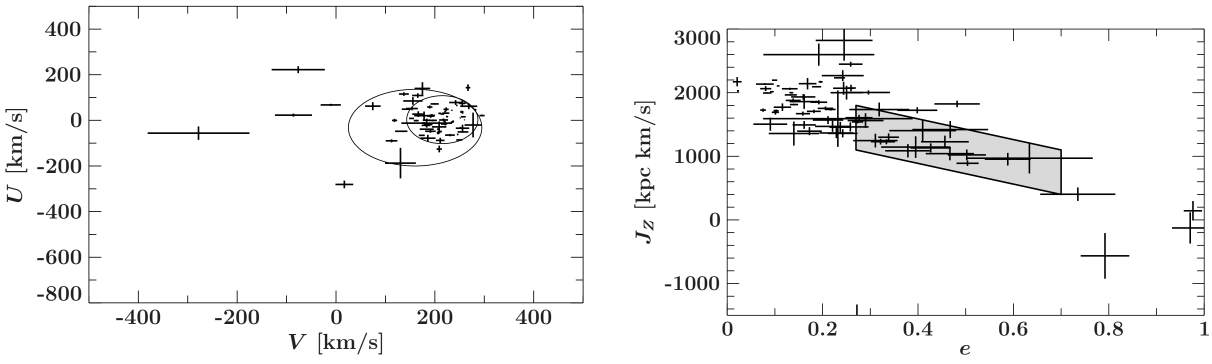

Figure 13: $U - V$ and $e - J_Z$ diagrams for the sdB sample in Model I

The sdO sample has the highest percentage of halo candidates with 21.9 % and the count for thick members is at 19.5 %. The majority also belongs to the thin disk population, but the percentage is significantly lower than the sdB sample with 58.5 %. The sdO sample mainly consist of single stars with 78.0 %. There is only one binary system with a cool companion which makes 2.4 % of the total sample and the percentage for close binary systems and RV variable stars is 7.3 %. The amount of possible retrograde orbits is the largest in the sdO sample. Overall only PG1047-066 and HE1356-1613 are identified as a retrograde orbit.

Table 7: Population distribution of binary systems in the sdO sample for Model I

sdO star	**halo**	**thick**	**thin**	**all**
single stars	7	5	20	32
cool companion	0	0	1	1
close binary	0	1	2	3
rv variable	2	2	1	5
all	9	8	24	41

Table 8: Charakterization values for halo and thick disk members of the SPY sdO sample in Model I

star	$\rho - z$	$U - V$	$e - J_Z$	**Model I**
HE 0040-4838	halo	halo	halo	halo
HE 1356-1613	halo	halo	halo	halo
HE 2218-2026	halo	halo	halo	halo
HE 2347-4130	halo	halo	halo	halo
PG 1047-066	halo	halo	halo	halo
PG 1251+019	halo	halo	halo	halo
PG 1430-083	halo	halo	halo	halo
PG 2204+070	halo	halo	halo	halo
GD104	thick	thick	thick	thick
EC11363-1641	halo	thick	thick	thick
EC14466-1058	thick	thick	thick	thick
HE1115-0631	thick	thin	thick	thick
HE1256-2738	halo	thick	halo	halo
PG0953+024	halo	thick	thick	thick
PG1237-141	halo	thin	thick	thick
TonS148	halo	thick	thick	thick
WD2020-253	thick	thin	thick	thick

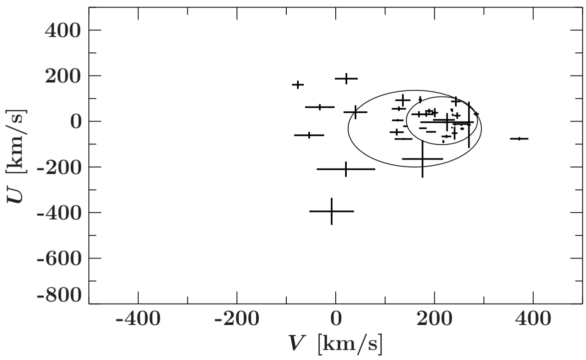

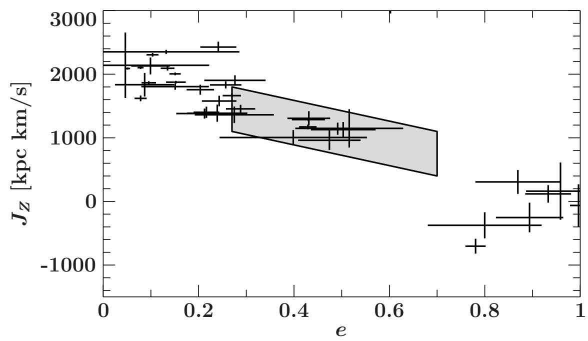

Figure 14: $U - V$ and $e - J_Z$ diagrams for the sdO sample in Model I

Table 9 shows the population distribution of different samples in percentage. The first two lines are the single stars of the SPY sdB sample and the close binary sample. The following lines are population distribution of other samples. Pauli et al. (2006) discussed 395 white dwarfs of the SPY sample. Martin et al. (2017) discussed 88 subluminous O and B stars and there is an overlap of 8 stars with the SPY sample. Their stellar classification matches for five stars with the classification of this research. They identified HE1135-1134, HE1238-1745 and TonS 133 as a member of the thick disk while these stars have been identified as part of the thin disk in this research. Martin et al. (2017) applied the same classification method on these stars, but had a loser definition for the thin disk.

Table 9: Distribution of stellar population in different samples in %

sample	**halo**	**thick**	**thin**
single sdB	11.9	26.2	61.9
close binaries	3.8	12.0	84.2
Pauli et al. (2006)	1.8	6.8	91.4
Martin et al. (2017)	8.0	40.9	51.1

8 Conclusion

The recent Data Release of the Gaia mission in April 2018 provided new stellar data for billions of stars. The direct measurements of parallaxes and proper motions from space based instruments have high precision which allow to minimize systematical errors even further. Compared to ground based measurements they are better by a factor of at least ten.

In a large scale analysis hot subdwarfs of type O and B have been in focus for this research, especially the SPY sdO and sdB sample and the close binary sample taken from Kupfer et al. (2015) which is a collection of binary systems with solved orbits. Radial velocities for both SPY samples have been taken from spectra of the SPY project. With an average of two spectra per star the resulting velocities hinted the existence of four new binary systems. The RV variable stars in the sdB sample are HE0016+0044 and HE0207+0030 and the variable ones in the sdO sample are WD2020-253 and PG0026+136.

The impact of the chosen mass model of our Galaxy has been investigated based on the results of the large scale kinematic analysis. Therefore, three common models for the gravitational potential of our Galaxy have been analyzed while determining the stellar population distribution of the mentioned samples. Overall, only 2.1 % of the stars have been identified of a different stellar population depending on the chosen mass model. Therefore, mass model I based on the Allen & Santillan (1991) is chosen for further investigations because it is of intermediate mass between model II and model III.

The stars of the SPY samples and the close binary sample have been categorized in different stellar populations with respect to their binarity. Therefore, the classification method is based on Pauli et al. (2006). Halo stars and thick disk stars of all samples are listed individually together with their classification values of the respective diagrams. The overall distribution is the same for all samples. However, the SPY sdO samples has a higher percentage of halo candidates with 21.9 % compared to other samples. While comparing the stellar classifications with the results of overlaping stars of Martin et al. (2017), only five out of eight stars have the same classification.

In order to eliminate uncertainties even more better stellar data is necessary. The measurements of the Gaia mission will improve with the next data release and therefore minimize current flaws like parallax measurements with significant large errors. Furthermore, the amount of binaries in hot subdwarf samples is high, but the information about solved orbits is low. Due to conservative approaches to circumvent unknown system velocities errors grow larger. When executed on kinematics the stellar population classifications will benefit from detailed solved orbits of future research.

A Kinematic Values

Table 10: Stellar data for stars of the SPY sdO and sdB sample with available parallaxes. Population indications are halo (H), thick disk (TK) and thin disk (TN). Type indications are systems with a cool companion from Lisker et al. (2005) (CL), from (Geier et al., 2011) (CM), close binary systems from Kupfer et al. (2015)(K) and new RV variable stars (RV)

star	**par [mas]**	$v_{rad}[\frac{km}{s}]$	**pmra [mas]**	**pmdec [mas]**	**pop**	**type**
LB275	0.8065 ± 0.0809	63.682 ± 2.4522	-3.783 ± .159	-9.437 ± 0.199	TN	
EC11363-1641	0.422 ± 0.0592	88.0 ± 3.3	-9.6 ± .1	-6.4 ± 0.1	TK	
EC14466-1058	0.5054 ± 0.0764	60.3 ± 3.2525	-3.895 ± .132	-11.241 ± 0.138	TK	
GD104	0.5813 ± 0.0886	100.309 ± 10.957	-6.583 ± .132	-9.344 ± 0.119	TK	
GD1237	0.409 ± 0.0686	-42.4 ± 4.225	12.453 ± .102	0.501 ± 0.085	TK	
GD617	0.435 ± 0.0525	-1.8 ± 1.0825	-7.084 ± .075	-9.163 ± 0.059	H	
GD619	1.2245 ± 0.0584	24 ± 5.965	-3.786 ± .086	-3.216 ± 0.052	TN	
HE0007-2212	0.7722 ± 0.0826	-3 ± 11.8375	0.151 ± .114	7.962 ± 0.088	TK	
HE0016+0044	0.5801 ± 0.0903	26.491 ± 0.6081	3.052 ± .199	-10.174 ± 0.097	TN	RV
HE0019-5545	0.6007 ± 0.0736	82.2 ± 3.522	4.978 ± .107	-11.19 ± 0.1	TK	
HE0031-5607	0.5317 ± 0.0588	0.65 ± 2.2525	7.159 ± .085	1.743 ± 0.085	TN	
HE0101-2707	0.8206 ± 0.0632	19.5 ± 1.46	-1.609 ± .083	-10.795 ± 0.076	TN	
HE0123-3330	0.7017 ± 0.0663	43.8 ± 1.465	14.01 ± .08	-0.552 ± 0.064	TN	
HE0135-6150	0.3016 ± 0.0513	29.55 ± 3.032	3.469 ± .097	0.906 ± 0.078	TN	
HE0151-3919	0.5884 ± 0.0396	-48.5 ± 0.52	-4.534 ± .04	-44.402 ± 0.046	H	
HE0155-3710	0.7665 ± 0.0463	-14.55 ± 8.425	12.057 ± .038	4.731 ± 0.056	TN	
HE0207+0030	0.5456 ± 0.0723	18.387 ± 11.8065	-4.012 ± .157	-0.425 ± 0.111	TN	RV
HE0321-0918	0.9257 ± 0.0648	35.5 ± 3.965	2.149 ± .118	-5.826 ± 0.123	TN	
HE0342-1702	0.8975 ± 0.0737	53.1953 ± 1.02425	-7.394 ± .09	-2.425 ± 0.06	TN	
HE0414-5429	0.5502 ± 0.0376	19.8 ± 2.3225	1.327 ± .08	3.372 ± 0.076	TN	
HE0513-2354	0.3125 ± 0.0569	80 ± 16.81	0.381 ± .073	6.101 ± 0.1	TN	
HE0539-4246	1.0874 ± 0.0335	53.7 ± 4.612	4.59 ± .064	9.639 ± 0.067	TN	
HE1021-0255	0.6669 ± 0.1009	42.25 ± 1	-12.903 ± .261	7.612 ± 0.356	TN	
HE1047-0436	0.7366 ± 0.0896	25.0 ± 3.0	-13.856 ± .148	0.806 ± 0.13	TN	
HE1050-0630	1.0975 ± 0.0718	-14.666 ± 1.5475	-10.176 ± .107	-5.209 ± 0.09	TN	
HE1136-2504	0.8709 ± 0.0567	59.75 ± 9.0625	-5.716 ± .108	-6.27 ± 0.062	TN	
HE1200-0931	0.4985 ± 0.0789	38.25 ± 3.782	-8.405 ± .179	-1.338 ± 0.097	TN	CL
HE1221-2618	0.7006 ± 0.0469	-15.3 ± 3.94	-12.373 ± .067	-2.493 ± 0.067	TN	CL
HE1238-1745	0.6906 ± 0.0724	-4.047 ± 0.159	-12.41 ± .139	4.218 ± 0.074	TN	
HE1254-1540	0.979 ± 0.0843	26.2 ± 7.3	-8.414 ± .174	-11.338 ± 0.129	TN	CL
HE1256-2738	0.5893 ± 0.1045	159.593 ± 24.3139	-21.336 ± .188	-4.602 ± 0.145	TK	
HE1310-2733	0.8459 ± 0.0606	39.2828 ± 14.4409	2.066 ± .108	-2.225 ± 0.093	TN	
HE1352-1827	0.5016 ± 0.0639	-49.55 ± 20.45	1.306 ± .121	-4.285 ± 0.096	TN	CL
HE1415-0309	0.5869 ± 0.0974	237.25 ± 18.125	-0.758 ± .173	-10.854 ± 0.147	TK	
HE1441-0558	1.3427 ± 0.0428	3.15 ± 1.632	-11.641 ± .068	-3.69 ± 0.061	TN	CL
HE1450-0957	0.7788 ± 0.0894	-48.784 ± 17.60118	-10.226 ± .179	-12.802 ± 0.156	TN	
HE1459-0234	0.8273 ± 0.0432	-38.8 ± 4.805	-7.589 ± .083	-15.356 ± 0.075	TK	
HE1519-0708	0.4026 ± 0.0919	16.05 ± 31.345	-2.291 ± .174	-2.961 ± 0.193	TN	
HE2156-3927	1.2584 ± 0.0746	-64.533 ± 1.222	4.509 ± .082	8.645 ± 0.088	TN	CL
HE2203-2210	0.6077 ± 0.0889	51.9 ± 5.0125	12.866 ± .14	-9.627 ± 0.133	TN	
HE2208+0126	0.8509 ± 0.0971	8.05 ± 1.0825	4.899 ± .142	0.838 ± 0.141	TN	
HE2218-2026	0.4426 ± 0.0772	-269.61 ± 0.6856	20.59 ± .138	-17.513 ± 0.13	H	
HE2222-3738	0.8303 ± 0.0585	-4.66 ± 6.647	8.896 ± .089	1.786 ± 0.08	TN	
HE2307-0340	0.7719 ± 0.0728	-23.95 ± 1.712	-3.921 ± .109	-9.585 ± 0.088	TN	
HE2322-0617	0.7588 ± 0.0807	25.85 ± 21.152	12.563 ± .13	1.881 ± 0.098	TN	CL
HE2322-4559	0.3786 ± 0.0658	-53.8 ± 1.565	9.472 ± .063	-5.903 ± 0.083	TK	CL
HE2347-4130	0.3706 ± 0.0544	4.6 ± 1	-20.728 ± .063	-31.226 ± 0.087	H	
HE2349-3135	0.4339 ± 0.0831	204.55 ± 3.92	9.928 ± .128	-3.971 ± 0.126	TK	
HS1530+0542	0.7651 ± 0.0277	10.85 ± 10.44	-19.578 ± .046	-12.458 ± 0.045	TK	
HS1536+0944	0.4063 ± 0.0712	-49.4 ± 1.44	-32.263 ± .116	-32.836 ± 0.168	H	CL
HS1710+1614	0.4366 ± 0.0699	3.35 ± 8.982	-2.84 ± .104	-3.502 ± 0.119	TN	
HS2033+0821	1.3832 ± 0.0532	1.55 ± 6.1	4.427 ± .083	0.413 ± 0.072	TN	

Table 10 – continued from previous page

star	**par [mas]**	$v_{rad}[\frac{km}{s}]$	**pmra [mas]**	**pmdec [mas]**	**pop**	**type**
HS2216+1833	1.1852 ± 0.0405	29.4 ± 2.21	-11.919 ± .058	-23.361 ± 0.053	TN	CL
HS2357+2201	1.0675 ± 0.083	-54.2 ± 0.722	5.517 ± .137	-11.984 ± 0.055	TN	
HZ1	3.0967 ± 0.0671	-4.5 ± 7.06	-6.033 ± .14	8.058 ± 0.065	TN	
KUV01542-0710	0.442 ± 0.0909	-38.8 ± 9.942	-0.834 ± .127	-8.719 ± 0.105	TN	CL
PG0258+184	0.6126 ± 0.0631	24.15 ± 5.765	8.611 ± .12	-4.728 ± 0.11	TN	CL
PG0953+024	0.3966 ± 0.0793	52.65 ± 0.9125	-16.155 ± .128	-8.474 ± 0.111	TK	
PG0958-119	0.6352 ± 0.0583	35.95 ± 0.5625	0.525 ± .096	2.418 ± 0.089	TN	
PG1207-032	1.7047 ± 0.0745	-5.95 ± 20.702	9.71 ± .136	-5.725 ± 0.104	TN	
PG1251+019	0.3646 ± 0.0715	49.7666 ± 5.81625	3.823 ± .156	-22.047 ± 0.087	H	
PG1258+012	0.4411 ± 0.0868	-26.2 ± 19.21	-10.519 ± .2	4.087 ± 0.125	TN	CM
PG1511-110	0.8493 ± 0.0674	40.67 ± 37.3799	0.204 ± .121	-1.853 ± 0.099	TN	
PG1549-001	0.5742 ± 0.0629	-8.05 ± 6.122	-16.706 ± .121	-1.256 ± 0.105	TK	
PG1632+223	0.5338 ± 0.0481	6.75 ± 1.96	-3.561 ± .062	-3.778 ± 0.072	TN	
PG2122+157	0.7993 ± 0.04	-120.2 ± 0.61	-9.475 ± .065	-0.747 ± 0.067	TK	CL
PG2204+070	8.1876 ± 0.1179	164.002 ± 24.825	-31.82 ± .177	-18.137 ± 0.164	H	
PHL555	1.4739 ± 0.074	-28.45 ± 1.025	15.798 ± .092	-3.581 ± 0.101	TN	
PHL932	3.215 ± 0.0756	9.15 ± 1.21	35.55 ± .138	5.688 ± 0.118	TN	
SB485	1.6614 ± 0.0654	-33.7 ± 6.6625	3.746 ± .165	4.576 ± 0.095	TN	
TonS133	0.5463 ± 0.0873	-85.557 ± 78.771	6.918 ± .127	-6.793 ± 0.105	TN	
TonS137	1.347 ± 0.0539	-11.6 ± 5.8	11.803 ± .13	-30.018 ± 0.061	TN	
TonS148	0.562 ± 0.0592	151.4 ± 1.332	5.987 ± .075	-14.219 ± 0.067	TK	
TONS155	0.1956 ± 0.0607	-21.35 ± 3.505	4.663 ± .101	-6.434 ± 0.087	H	CL
WD2020-253	0.4286 ± 0.0803	124.720 ± 0.4249	-8.845 ± .122	-10.825 ± 0.079	TK	RV
WD2258+155	0.7442 ± 0.078	-33.225 ± 20.190	-7.144 ± .152	1.946 ± 0.094	TN	

Table 11: Stellar data for stars of the close binary sample with available parallaxes. Population indications are halo (H), thick disk (TK) and thin disk (TN)

star	**par [mas]**	$v_{rad}[\frac{km}{s}]$	**pmra [mas]**	**pmdec [mas]**	**pop**
2M1533+3759	1.9007 ± 0.0476	-3.4 ± 5.2	0.012 ± 0.074	-17.025 ± 0.096	TN
2M1938+4603	2.4952 ± 0.0404	20.1 ± 0.3	5.196 ± 0.077	-4.638 ± 0.077	TN
AADor	2.7188 ± 0.0588	1.57 ± 0.09	-12.109 ± 0.096	51.071 ± 0.122	TN
BULSC16335	0.8046 ± 0.0988	36.4 ± 19.6	-0.312 ± 0.177	-1.142 ± 0.147	TN
CD-24731	4.2702 ± 0.0792	20.0 ± 5.0	84.514 ± 0.129	-47.35 ± 0.085	TN
CD-3011223	2.9629 ± 0.0797	16.5 ± 0.3	6.214 ± 0.165	-6.411 ± 0.22	TN
CPD-201123	3.011 ± 0.0633	-6.3 ± 1.2	6.429 ± 0.08	-17.327 ± 0.136	TN
CPD-64481	4.3779 ± 0.0323	94.1 ± 0.3	-3.017 ± 0.064	-29.304 ± 0.068	TN
CS1246	1.4839 ± 0.0254	67.2 ± 1.7	-17.292 ± 0.034	-0.212 ± 0.034	TN
EC00404-4429	1.5217 ± 0.0507	33.0 ± 2.9	23.074 ± 0.056	10.712 ± 0.07	TN
EC02200-2338	3.2311 ± 0.0578	20.7 ± 2.3	29.987 ± 0.1	-14.169 ± 0.1	TN
EC12408-1427	2.1212 ± 0.0758	-52.2 ± 1.2	-22.947 ± 0.145	7.547 ± 0.096	TN
EC13332-1424	1.3333 ± 0.1158	-53.2 ± 1.8	-9.124 ± 0.13	15.83 ± 0.118	TN
EC20182-6534	1.5762 ± 0.0486	13.5 ± 1.9	-12.133 ± 0.049	-7.867 ± 0.07	TN
EC20260-4757	1.4676 ± 0.0541	56.6 ± 1.6	-1.557 ± 0.075	-1.185 ± 0.068	TN
EC20369-1804	1.101 ± 0.0765	7.2 ± 1.6	8.519 ± 0.119	-4.5 ± 0.074	TN
EC21556-5552	1.866 ± 0.0521	31.4 ± 2.0	2.119 ± 0.072	5.107 ± 0.077	TN
EC22202-1834	1.0914 ± 0.066	-5.5 ± 3.9	9.636 ± 0.117	-15.73 ± 0.114	TN
EGB5	1.673 ± 0.0789	68.5 ± 0.7	-17.215 ± 0.138	5.279 ± 0.084	TN
Feige108	2.4898 ± 0.0967	45.8 ± 0.6	-0.157 ± 0.148	-15.489 ± 0.134	TN
Feige48	1.2162 ± 0.0394	-47.9 ± 0.1	-25.921 ± 0.064	-7.395 ± 0.062	TK
GALEXJ0321+4727	3.7627 ± 0.0579	69.6 ± 2.2	58.796 ± 0.116	-8.241 ± 0.091	TN
GALEXJ2349+3844	4.0076 ± 0.0639	2.0 ± 1.0	-2.203 ± 0.088	1.135 ± 0.066	TN
GD687	1.1214 ± 0.055	32.3 ± 3.0	-2.547 ± 0.062	-14.15 ± 0.068	TN
HD171858	7.4122 ± 0.0811	62.5 ± 0.1	-18.945 ± 0.122	-21.659 ± 0.102	TN
HE0230-4323	1.0739 ± 0.0676	16.6 ± 1.0	-6.687 ± 0.086	-6.425 ± 0.097	TN
HE0532-4503	0.3444 ± 0.0555	8.5 ± 0.1	1.933 ± 0.109	-1.976 ± 0.109	TN
HE0929-0424	0.5882 ± 0.1067	41.4 ± 1.0	-1.518 ± 0.147	1.851 ± 0.16	TN
HE1047-0436	0.7366 ± 0.0896	25.0 ± 3.0	-13.856 ± 0.148	0.806 ± 0.13	TN

Table 11 - continued from previous page

star	**par [mas]**	$v_{rad}[\frac{km}{s}]$	**pmra [mas]**	**pmdec [mas]**	**pop**
HE1059-2735	0.3684 ± 0.0667	-44.7 ± 0.6	-9.614 ± 0.112	1.78 ± 0.09	TN
HE1115-0631	0.7817 ± 0.0734	87.1 ± 1.3	-9.2812 ± 0.1401	-6.3198 ± 0.08126	TH
HE1318-2111	0.6139 ± 0.0709	48.9 ± 0.7	2.995 ± 0.122	-3.012 ± 0.107	TN
HE1414-0309	0.5869 ± 0.0974	104.7 ± 9.5	-0.758 ± 0.173	-10.854 ± 0.147	TK
HE1448-0510	0.9371 ± 0.0537	-45.5 ± 0.8	-4.235 ± 0.117	-5.805 ± 0.099	TN
HE2135-3749	1.7302 ± 0.0576	45.0 ± 0.5	24.598 ± 0.078	-0.303 ± 0.071	TN
HE2150-0238	0.8967 ± 0.0977	-32.5 ± 0.9	5.031 ± 0.153	-4.64 ± 0.159	TN
HS0705+6700	0.8056 ± 0.0498	-36.4 ± 2.9	-0.409 ± 0.061	-7.637 ± 0.07	TN
HS1741+2133	1.0363 ± 0.0351	-112.8 ± 2.7	-11.414 ± 0.032	3.216 ± 0.061	TK
HS2333+3927	0.7885 ± 0.0497	-31.4 ± 2.1	1.96 ± 0.069	-2.397 ± 0.051	TN
HWVir	5.7972 ± 0.0849	-13.0 ± 0.8	8.969 ± 0.175	-15.677 ± 0.107	TN
J002323-002953	0.5486 ± 0.0852	16.4 ± 2.1	27.246 ± 0.19	10.659 ± 0.104	H
J011857-002546	0.6356 ± 0.0733	37.7 ± 1.8	0.684 ± 0.181	-4.476 ± 0.08	TN
J012022+395059	0.6037 ± 0.0707	-47.3 ± 1.3	1.585 ± 0.115	-1.405 ± 0.104	TN
J032138+053840	1.1971 ± 0.0722	-16.7 ± 2.1	4.701 ± 0.142	-5.795 ± 0.127	TN
J082053+000843	0.6609 ± 0.0632	9.5 ± 1.3	0.567 ± 0.098	-2.1 ± 0.063	TN
J095101+034757	0.4064 ± 0.0981	111.1 ± 2.5	-11.717 ± 0.123	-8.057 ± 0.111	TK
J095238+625818	0.8899 ± 0.051	-35.4 ± 3.6	0.756 ± 0.051	-5.785 ± 0.066	TN
J113241-063652	0.5323 ± 0.0852	8.3 ± 2.2	-8.513 ± 0.148	-2.041 ± 0.095	TN
J113840-003531	0.8649 ± 0.063	23.3 ± 3.7	-8.426 ± 0.117	-25.372 ± 0.07	TK
J134632+281722	0.7389 ± 0.0457	1.2 ± 1.2	-12.104 ± 0.079	-6.705 ± 0.048	TK
J150513+110836	0.8378 ± 0.0905	-77.1 ± 1.2	-18.501 ± 0.129	-23.758 ± 0.113	TK
J162256+473051	0.4672 ± 0.0562	-54.7 ± 1.5	-3.406 ± 0.106	-2.223 ± 0.128	TN
J165404+303701	0.6985 ± 0.0455	40.5 ± 2.2	2.809 ± 0.069	-10.563 ± 0.104	TN
J172624+274419	0.6674 ± 0.054	-36.7 ± 4.8	2.363 ± 0.081	-15.598 ± 0.092	TN
J183249+630910	0.3625 ± 0.0517	-32.5 ± 2.1	1.806 ± 0.129	-0.156 ± 0.108	TN
J192059+372220	0.3987 ± 0.0488	16.8 ± 2.0	-2.15 ± 0.079	-2.809 ± 0.082	TN
J225638+065651	0.9258 ± 0.0658	-7.3 ± 2.1	-4.414 ± 0.114	-3.108 ± 0.079	TN
JL82	2.271 ± 0.0701	-1.6 ± 0.8	17.408 ± 0.091	-17.581 ± 0.111	TN
KBS13	1.7263 ± 0.038	7.53 ± 0.08	2.581 ± 0.062	-8.881 ± 0.062	TN
KIC10553698	0.7437 ± 0.0328	52.1 ± 1.5	-4.185 ± 0.057	2.956 ± 0.058	H
KIC11558725	0.7931 ± 0.0334	-66.1 ± 1.4	-6.727 ± 0.064	-11.967 ± 0.066	TN
KIC7668647	0.732 ± 0.0393	-27.4 ± 1.3	-2.02 ± 0.07	-6.091 ± 0.066	TN
KPD0025+5402	1.3937 ± 0.0365	-7.8 ± 0.7	-3.03 ± 0.04	-11.284 ± 0.04	TN
KPD0422+5421	1.4634 ± 0.0373	-57.0 ± 12	4.288 ± 0.047	-9.028 ± 0.037	TN
KPD1930+2752	1.1411 ± 0.0492	5.0 ± 1.0	1.744 ± 0.072	-0.499 ± 0.089	TN
KPD1946+4340	0.9264 ± 0.0358	-5.5 ± 1.0	-0.643 ± 0.063	-4.618 ± 0.064	TN
KPD2040+3955	1.2506 ± 0.041	-16.4 ± 1.0	-12.12 ± 0.061	-13.987 ± 0.074	TN
KPD2215+5037	1.5771 ± 0.0516	-7.2 ± 1.0	4.684 ± 0.083	10.756 ± 0.076	TN
KUV16256+4034	2.4234 ± 0.0435	-90.9 ± 0.9	-17.943 ± 0.068	-14.995 ± 0.083	TN
LB1516	1.8868 ± 0.0677	14.3 ± 1.1	6.46 ± 0.059	1.216 ± 0.082	TN
NSVS14256825	1.1929 ± 0.0599	12.1 ± 1.5	8.063 ± 0.09	1.133 ± 0.062	TN
PB5333	2.1846 ± 0.0541	-95.3 ± 1.3	25.785 ± 0.112	-21.136 ± 0.07	TK
PB7352	2.168 ± 0.0661	-2.1 ± 0.3	2.387 ± 0.104	3.707 ± 0.095	TN
PG0001+275	1.8011 ± 0.0556	-44.7 ± 0.5	4.43583 ± 0.07129	-19.186 ± 0.03413	TN
PG0101+039	2.6562 ± 0.122	7.3 ± 0.2	11.057 ± 0.16	-29.354 ± 0.09	TN
PG0133+114	3.352 ± 0.1155	-0.3 ± 0.2	23.009 ± 0.147	-24.415 ± 0.123	TN
PG0839+399	0.8345 ± 0.0611	23.2 ± 1.1	2.199 ± 0.084	-6.834 ± 0.064	TN
PG0849+319	0.9319 ± 0.0760	64.0 ± 1.5	-9.5713 ± 0.10332	-5.8660 ± 0.07451	TN
PG0850+170	1.1452 ± 0.0644	32.2 ± 2.8	4.097 ± 0.11	-4.936 ± 0.077	TN
PG0907+123	0.9761 ± 0.0559	56.3 ± 1.1	-5.701 ± 0.117	-0.003 ± 0.118	TN
PG0918+029	1.9777 ± 0.0493	104.4 ± 1.7	-25.512 ± 0.09	-20.601 ± 0.071	TK
PG0919+273	2.9273 ± 0.0801	-68.6 ± 0.6	23.343 ± 0.113	-27.557 ± 0.081	TN
PG0934+186	1.7337 ± 0.0937	7.7 ± 3.2	-13.711 ± 0.15	-10.151 ± 0.124	TN
PG0940+068	1.2443 ± 0.0771	-16.7 ± 1.4	8.83616 ± 0.12257	-5.0680 ± 0.11172	TN
PG0941+280	1.5012 ± 0.0731	73.7 ± 4.3	-16.304 ± 0.173	-40.508 ± 0.24	TK
PG0958-073	1.9106 ± 0.0601	90.5 ± 0.8	-42.368 ± 0.092	-1.876 ± 0.086	TN
PG1000+408	1.0058 ± 0.0474	56.6 ± 3.4	-2.169 ± 0.062	-19.271 ± 0.066	TK
PG1017-086	0.8963 ± 0.0955	-9.1 ± 1.3	-4.611 ± 0.133	8.299 ± 0.119	TN

Table 11 - continued from previous page

star	par [mas]	$v_{rad}[\frac{km}{s}]$	pmra [mas]	pmdec [mas]	pop
PG1032+406	4.5872 ± 0.0894	24.5 ± 0.5	-79.217 ± 0.14	-43.094 ± 0.112	TN
PG1043+760	1.408 ± 0.0375	24.8 ± 1.4	1.75 ± 0.079	-0.116 ± 0.069	TN
PG1101+249	2.3076 ± 0.0641	-0.8 ± 0.9	-26.773 ± 0.115	18.201 ± 0.094	TN
PG1110+294	1.2236 ± 0.0685	-15.2 ± 0.9	-6.046 ± 0.116	-9.076 ± 0.136	TN
PG1116+301	1.2154 ± 0.0779	-0.2 ± 1.1	-14.928 ± 0.139	-12.116 ± 0.231	TN
PG1230+052	1.605 ± 0.0692	-43.1 ± 0.7	-10.776 ± 0.144	-14.02 ± 0.097	TN
PG1232-136	1.9935 ± 0.0757	4.1 ± 0.3	-46.527 ± 0.154	6.786 ± 0.092	TN
PG1244+113	0.9736 ± 0.0824	7.4 ± 0.8	4.488 ± 0.162	-0.339 ± 0.077	TN
PG1247+554	4.0815 ± 0.0555	13.8 ± 0.6	-66.921 ± 0.08	-12.317 ± 0.078	TN
PG1248+164	1.2001 ± 0.0575	-16.2 ± 1.3	9.265 ± 0.102	-10.556 ± 0.071	TN
PG1300+279	0.8721 ± 0.0557	-3.1 ± 0.9	-5.396 ± 0.081	-5.667 ± 0.065	TN
PG1329+159	1.2376 ± 0.0551	-22.0 ± 1.2	-23.199 ± 0.112	-15.99 ± 0.054	TN
PG1336-018	1.8116 ± 0.0632	-25.0 ± 5.0	-6.112 ± 0.127	-11.914 ± 0.093	TN
PG1403+316	1.6770 ± 0.0598	-2.1 ± 0.9	-30.745 ± 0.10132	1.89861 ± 0.10758	TN
PG1432+159	1.5968 ± 0.08	-16.0 ± 1.1	7.361 ± 0.101	-26.493 ± 0.104	TN
PG1439-013	0.7738 ± 0.0621	-53.7 ± 1.6	-9.069 ± 0.154	-0.437 ± 0.108	TN
PG1452+198	3.1492 ± 0.0672	-9.1 ± 2.1	-0.693 ± 0.103	-18.926 ± 0.115	TN
PG1512+244	2.0792 ± 0.0377	-2.9 ± 1.0	-39.142 ± 0.067	2.943 ± 0.07	TN
PG1519+640	2.772 ± 0.0418	0.1 ± 0.4	24.593 ± 0.094	31.293 ± 0.09	TK
PG1528+104	1.4704 ± 0.047	-49.3 ± 1.0	-18.355 ± 0.073	-10.644 ± 0.073	TN
PG1558-007	1.4818 ± 0.0458	-71.9 ± 0.7	-12.378 ± 0.081	-6.336 ± 0.061	TN
PG1619+522	2.0065 ± 0.0463	-52.5 ± 1.1	-4.86 ± 0.079	9.901 ± 0.107	TN
PG1648+536	1.1335 ± 0.0361	-69.9 ± 0.9	-1.235 ± 0.065	-21.954 ± 0.09	TN
PG1725+252	1.67 ± 0.0463	-60.0 ± 0.6	-18.337 ± 0.067	6.183 ± 0.071	TN
PG1743+477	1.3047 ± 0.0286	-65.8 ± 0.8	1.518 ± 0.058	12.023 ± 0.065	TN
PG2331+038	0.9284 ± 0.0559	-9.5 ± 1.1	-11.737 ± 0.097	-15.518 ± 0.067	TN
PG2345+318	1.2493 ± 0.0566	-10.6 ± 1.4	4.199 ± 0.127	-3.468 ± 0.054	TN
PHL861	0.7972 ± 0.0667	-26.5 ± 0.4	1.729 ± 0.118	-27.214 ± 0.092	TK
TONS135	1.4368 ± 0.0571	-3.7 ± 1.1	6.714 ± 0.103	-18.625 ± 0.066	TN
TONS183	1.9993 ± 0.0561	50.5 ± 0.8	-6.803 ± 0.081	-14.365 ± 0.074	TN
UVEX0328+5035	1.6587 ± 0.0322	44.9 ± 0.7	-5.31 ± 0.062	-4.6 ± 0.057	TN
UVO1419-09	3.2108 ± 0.0906	42.3 ± 0.3	-8.362 ± 0.128	-39.569 ± 0.123	TN
UVO1735+22	2.2251 ± 0.05	20.6 ± 0.4	-21.658 ± 0.055	1.37 ± 0.084	TN
V1093Her	1.14 ± 0.0342	-3.9 ± 0.8	6.441 ± 0.071	-22.62 ± 0.072	TN
V1405Ori	1.402 ± 0.0383	-33.6 ± 5.5	0.897 ± 0.071	-6.695 ± 0.037	TN
V2579Oph	1.7223 ± 0.0713	-54.16 ± 0.27	-5.337 ± 0.086	-14.395 ± 0.062	TN

Table 12: Stellar data for stars of the SPY sdO, sdB and close binary sample without available parallaxes. Population indications are halo (H), thick disk (TK) and thin disk (TN). Type indications are systems with a cool companion from Lisker et al. (2005) (CL), close binary systems from Kupfer et al. (2015) (K) and new RV variable stars (RV)

star	distance[kpc]	v_{rad} or $\gamma[\frac{km}{s}]$	pmra [mas]	pmdec [mas]	pop	type
HE0040-4838	2.7773 ± 0.3239	81 ± 4.85	16.258 ± 0.076	-14.857 ± 0.09	H	
HE0136-2758	2.8 ± 0.3	-95.5 ± 5.245	19.468 ± 0.141	-18.704 ± 0.063	H	
HE0306-0309	1.9 ± 0.2	20.3 ± 10.625	0.706 ± 0.161	-4.161 ± 0.145	TN	
HE0415-2417	5.6 ± 0.6	188 ± 6.3325	7.121 ± 0.105	-4.351 ± 0.118	H	
HE1033-2353	2.6 ± 0.3	31.7 ± 4.2125	-2.189 ± 0.164	-0.882 ± 0.153	TN	
HE1140-0500	3.1356 ± 0.36717	-55 ± 6.646	-4.681 ± 0.124	-6.863 ± 0.063	TN	CL
HE1142-2311	1.9926 ± 0.23146	13.6 ± 9.685	-3.988 ± 0.193	-6.629 ± 0.099	TN	
HE1309-1102	2.8798 ± 0.33958	10.35 ± 5.952	-4.413 ± 0.213	-3.114 ± 0.156	TN	CL
HE1356-1613	2.5175 ± 0.2942	155.39 ± 22.259	-12.262 ± 0.257	-18.119 ± 0.259	H	
HE1407+0033	2.4 ± 0.2	-62.1 ± 11.545	-4.589 ± 0.137	-4.567 ± 0.111	TN	
HE1419-1205	2.5229 ± 0.29615	-72.55 ± 6.562	-12.427 ± 0.155	8.377 ± 0.123	H	CL
HE1422-1851	4.7688 ± 0.56035	27.15 ± 9.302	-9.079 ± 0.185	-4.054 ± 0.153	TK	CL
HE1519-0708	2.3 ± 0.2	16.05 ± 31.345	-2.291 ± 0.174	-2.961 ± 0.193	TN	
HE2151-1001	2.2 ± 0.2	-15.95 ± 11.38	13.511 ± 0.182	-5.493 ± 0.163	TK	
HE2201-0001	2.7 ± 0.3	-68.85 ± 10.812	-4.212 ± 0.159	-2.785 ± 0.165	TN	

Table 12 – continued from previous page

star	**distance[kpc]**	v_{rad} **or** $\gamma[\frac{km}{s}]$	**pmra [mas]**	**pmdec [mas]**	**pop**	**type**
HE2237+0150	2.7 ± 0.3	-74.05 ± 2.562	3.886 ± 0.161	-4.883 ± 0.136	TK	
HE2238-1455	3.0 ± 0.3	-97.45 ± 2.412	7.006 ± 0.139	-2.813 ± 0.124	TK	
HS2125+1105	2.4877 ± 0.29134	-1.25 ± 5.762	-0.915 ± 0.151	-11.464 ± 0.166	TN	CL
PG0026+136	3.206 ± 0.37277	14.40 ± 6.77	-0.724 ± 0.158	-4.816 ± 0.08	TN	RV
PG1047-066	3.2785 ± 0.38136	302.25 ± 5.8325	-13.56 ± 0.114	-9.734 ± 0.084	H	
PG1135-116	2.0151 ± 0.23542	34.40 ± 32.651	-6.012 ± 0.131	1.171 ± 0.079	TN	
PG1203-108	1.8449 ± 0.44552	-16.65 ± 4.24	-1.584 ± 0.162	-0.015 ± 0.102	TN	
PG1237-141	3.813 ± 0.44491	63.15 ± 4.0925	-10.484 ± 0.19	1.519 ± 0.104	TK	
PG1423-013	4.7721 ± 0.55776	-21.95 ± 24.6025	-2.695 ± 0.191	1.354 ± 0.159	TN	
PG1430-083	4.529 ± 0.5295	-67.5 ± 7.5125	-14.254 ± 0.127	-5.217 ± 0.105	H	
PG1513-045	2.0737 ± 0.24172	27.6 ± 25.4525	-11.453 ± 0.184	3.003 ± 0.219	TN	
TONS155	4.2935 ± 0.50474	-21.35 ± 3.505	4.663 ± 0.101	-6.434 ± 0.087	H	CL
HE1421-1206	1.72 ± 0.18	-86.2 ± 1.1	-10.294 ± 0.186	-5.411 ± 0.163	TN	
HS2043+0615	2.02 ± 0.20	43.5 ± 3.4	-2.732 ± 0.091	-6.342 ± 0.076	TN	
HS2359+1942	2.02 ± 0.26	-96.1 ± 6.0	-7.925 ± 0.119	-0.477 ± 0.1	TN	
J082332+113641	2.48 ± 0.22	135.1 ± 2.0	-3.858 ± 0.193	-1.877 ± 0.113	TK	K
J083006+475150	2.44 ± 0.27	49.9 ± 0.9	-4.015 ± 0.124	-7.002 ± 0.092	TK	K
J102151+301011	5.74 ± 0.55	-28.4 ± 4.8	-1.126 ± 0.311	-9.027 ± 0.302	H	K
J150829+494050	3.83 ± 0.41	-60.0 ± 10.7	-1.351 ± 0.155	-3.043 ± 0.26	TN	
J152222-013018	3.8324 ± 0.69038	-79.5 ± 2.7	-11.779 ± 0.275	-11.571 ± 0.214	H	K
J204613-045418	2.81 ± 0.33	87.6 ± 5.7	1.356 ± 0.12	-7.379 ± 0.082	TN	

B List of Figures and Tables

List of Figures

List of Tables

C Bibliography

Allen C., Santillan A., 1991, Rev. Mexicana Astron. Astrofis.22, 255

Geier S., Hirsch H., Tillich A., et al., 2011, A&A530, A28

Hirsch H., 2006, Heisse unterleuchtkraeftige Sterne aus dem Sloan Digital Sky Survey

Irrgang A., Wilcox B., Tucker E., Schiefelbein L., 2013, A&A549, A137

Kupfer T., Geier S., Heber U., et al., 2015, A&A576, A44

Lisker T., Heber U., Napiwotzki R., et al., 2005, A&A430, 223

Martin P., Jeffery C.S., Naslim N., Woolf V.M., 2017, MNRAS467, 68

Maxted P.F.L., Heber U., Marsh T.R., North R.C., 2001, MNRAS326, 1391

Napiwotzki R., Christlieb N., Drechsel H., et al., 2003, The Messenger 112, 25

Napiwotzki R., Karl C., Lisker T., et al., 2004, Astrophysics and Space Science 291, 321

Pauli E.M., 2003, 3D kinematics of white dwarfs from the SPY project

Pauli E.M., Napiwotzki R., Heber U., et al., 2006, A&A447, 173

Stroeer A., Heber U., Lisker T., et al., 2007, A&A462, 269

D Erklärung

Hiermit versichere ich, dass ich die vorliegende Arbeit selbstständig verfasst und keine anderen als die angegebenen Quellen und Hilfsmittel benutzt habe, dass alle Stellen der Arbeit, die wörtlich oder singemäß aus anderen Quellen übernommen wurden, als solche kenntlich gemacht sind und dass die Arbeit in gleicher oder ähnlicher Form noch keiner Prüfungsbehörde vorgelegt wurde.

Erlangen, den 2. November 2018